CrossMark

Accounting for Fault Roughness in Pseudo-Dynamic Ground-Motion Simulations

P. Martin Mai,[1] Martin Galis,[1] Kiran K. S. Thingbaijam,[1] Jagdish C. Vyas,[1] and Eric M. Dunham[2]

Abstract—Geological faults comprise large-scale segmentation and small-scale roughness. These multi-scale geometrical complexities determine the dynamics of the earthquake rupture process, and therefore affect the radiated seismic wavefield. In this study, we examine how different parameterizations of fault roughness lead to variability in the rupture evolution and the resulting near-fault ground motions. Rupture incoherence naturally induced by fault roughness generates high-frequency radiation that follows an ω^{-2} decay in displacement amplitude spectra. Because dynamic rupture simulations are computationally expensive, we test several kinematic source approximations designed to emulate the observed dynamic behavior. When simplifying the rough-fault geometry, we find that perturbations in local moment tensor orientation are important, while perturbations in local source location are not. Thus, a planar fault can be assumed if the local strike, dip, and rake are maintained. We observe that dynamic rake angle variations are anti-correlated with the local dip angles. Testing two parameterizations of dynamically consistent Yoffe-type source-time function, we show that the seismic wavefield of the approximated kinematic ruptures well reproduces the radiated seismic waves of the complete dynamic source process. This finding opens a new avenue for an improved pseudo-dynamic source characterization that captures the effects of fault roughness on earthquake rupture evolution. By including also the correlations between kinematic source parameters, we outline a new pseudo-dynamic rupture modeling approach for broadband ground-motion simulation.

Key words: Earthquake rupture dynamics, fault-surface roughness, physics-based ground-motion simulations, near-fault shaking, seismic hazard.

[1] Division of Physical Science and Engineering, King Abdullah University of Science and Technology, Thuwal 23955-6900, Kingdom of Saudi Arabia. E-mail: martin.mai@kaust.edu.sa
[2] Department of Geophysics, Stanford University, 397 Panama Mall, Stanford, CA 94305, USA.

1. Introduction

Standard ground-motion estimation procedures for seismic hazard assessment utilize empirical methods. The underlying empirical models, known as ground-motion prediction equations (GMPEs), are developed from strong-motion recordings of past earthquakes. They are used to quantify the expected shaking level for an earthquake of given magnitude, at some selected source-to-site distance, potentially involving additional parameters for source and site properties (e.g., Power et al. 2008; Mai 2009; Bozorgnia et al. 2014). The reliability of such empirical models critically depends on the input dataset, that is, the available strong-motion records and related metadata. However, strong-motion databases are limited, in particular for near-field observations of large ($M > 7$) earthquakes. Therefore, developing region-specific GMPEs is still difficult for most of the seismogenic regions across the globe. To overcome this limitation, recordings from several tectonic regimes are combined under the ergodicity assumption that earthquake source properties and seismic wave propagation effects either are identical or can be accounted for (e.g., Anderson and Brune 1999; Delavaud et al. 2012; Stewart et al. 2015). It is then necessary to justify the appropriateness of the GMPE for region-specific applications based on pre-specified selection criteria (e.g., Bommer et al. 2010), or to apply corrections before using them for different seismotectonic conditions (e.g., Campbell 2003; Bora et al. 2014).

Due to the increase in strong-motion instrumentation, and consequently increasing numbers of reliably recorded data and metadata, current GMPEs can be considered well constrained in the distance range 20–30 km for moderate (M 6–6.5) earthquakes (Chiou et al. 2008; Akkar et al. 2014; Ancheta et al.

2014). However, data coverage remains sparse for larger earthquakes ($M > 7$), especially at closer distances ($R < 20$ km). Therefore, GMPEs for this magnitude-distance range are unreliable, while independent testing of the corresponding GMPE predictions requires either many more earthquake recordings (available only in future decades) or advanced physics-based numerical simulations. We remark that typically GMPEs have been found to well constrain the median value of a chosen ground-motion parameter (e.g., peak ground velocity, PGV, or spectral acceleration at some period T, SA_T), while the variability (so-called sigma, σ) is often not well quantified. Therefore, GMPE-based near-source shaking estimation for large earthquakes is highly uncertain, in particular for long return periods for which ground-motion variability drives the seismic hazard (e.g., Bommer and Abrahamson 2006; Strasser et al. 2009) As a result, the earthquake engineering and seismological communities continue to discuss how to parameterize, improve, and select GMPEs for probabilistic seismic hazard assessment (PSHA) (e.g., Wang and Zhou 2007; Kluegel 2007).

To overcome the limitations of empirical equations for ground-motion prediction, simulation-based approaches are increasingly used. Pragmatic approaches are built on stochastic point-source simulations, potentially extended to account for finite-source effects (e.g., Atkinson et al. 2009); however, these methods ignore 3D wave propagation effects and the known complexity of the earthquake rupture process. More realistic methods include the complete physics of seismic wave excitation and propagation in realistic three-dimensional Earth models. For instances, using a kinematic rupture model (by a priori specifying fault displacement, rupture propagation and local slip rate function) in combination with a modern wave propagation solver allows accounting for 3D geologic structure and rupture complexities (e.g., Mai et al. 2010; Graves and Pitarka 2010, 2016; Roten et al. 2014).

A further refinement in ground-motion simulation invokes ab initio computations of the dynamic rupture process, starting from stress and friction on a possibly geometrically complex fault surface embedded in a 3D Earth model. Such computationally expensive simulations provide physics-based self-consistent rupture evolution and associated seismic radiation (e.g., Day 1982; Oglesby and Day 2002; Ripperger et al. 2007, 2008). This latter approach is physically desirable, but computationally more demanding than kinematic ground-motion calculations. Therefore, Guatteri et al. (2004) developed the first so-called pseudo-dynamic approach, based on correlations between dynamic source quantities (e.g., stress drop, fracture energy, slip-weakening distance) and the resulting kinematic rupture parameters (slip, peak slip rate, rise time, local rupture onset time). Subsequently, Schmedes et al. (2010) and Mena et al. (2012) extended and refined this first pseudo-dynamic model based on large sets of additional dynamic rupture simulations for different parameterizations of the initial dynamic source quantities. Other studies focused on understanding in more detail the correlations between earthquake source parameters (e.g., Schmedes 2013; Song and Somerville 2010; Song et al. 2013; Causse and Song 2015).

In this context, pseudo-dynamic means that the kinematic rupture process, quantified in terms of slip, slip rate, slip duration (rise time), and rupture onset time (related to rupture speed) at each point of the fault are specified according to principles of earthquake dynamics. In addition, the local source-time function (STF) needs to be specified, which is often done using the "classic" Brune parameterization (Brune 1970), while more recent parameterizations emulate the characteristics of the Kostrov function (Kostrov 1964) or Yoffe function (Yoffe 1951) (e.g., Tinti et al. 2005; Dreger 2007; Liu et al. 2006; see Mena et al. 2010 for a review). Ideally, any such pseudo-dynamic source parameterization is obtained from a wide range of dynamic rupture simulations. In this case, pseudo-dynamic source models capture the essential earthquake rupture physics, but are still inherently kinematic representations of the rupture process. Limitations in current pseudo-dynamic source modeling are related to simple planar fault geometry (no segmentation) in the underlying dynamic simulations, leading to rather smooth rupture evolution and inefficient radiation of higher frequencies, although empirical corrections for this shortcoming have been proposed (e.g., Graves and Pitarka 2010, 2016). The advantage of a pseudo-dynamic source characterization is that it limits running

costly (in terms of CPU requirements) numerical simulations for ground-motion simulations. The largest computational advantage arises for solving problems with many sources but few receivers. In this case, one can exploit reciprocity to obtain synthetic seismograms, leading to many orders of magnitude fewer simulations than when only solving forward problems. This approach is used, for instance, in the CyberShake approach (Graves et al. 2011), and it is also coded into a widely used implementation of the frequency–wave number integration method (Spudich and Xu 2003).

Earthquake-bearing faults contain structural (geometrical) complexities over a wide range of size scales, comprising large-scale features such fault segmentation and fault branches (e.g., Ben-Zion and Sammis 2003; Bistacchi et al. 2011) as well as small-scale fault roughness, that is, topographic variations of the fault surface (e.g., Power and Tullis 1991; Renard et al. 2006; Sagy et al. 2007; Sagy and Brodsky 2009; Candela et al. 2009, 2012). For large-scale geometrical complexity, we use the terminology of fault segmentation, whereby an earthquake is composed of several deterministically known rupture surfaces. In this study, we do not consider fault segmentation effects on rupture dynamics and near-field seismic radiation described elsewhere (e.g., Aochi and Madariaga 2003; Aochi and Douglas 2006; Oglesby et al. 2008; Oglesby and Mai 2012; Aochi and Ulrich 2015). On the other hand, small-scale roughness is not known deterministically, but well characterized statistically from field observations (e.g., Candela et al. 2009, 2012) and seismological models (Causse et al. 2010; Mai and Beroza 2002; Lavallee et al. 2006).

In our study, we aim to extend the pseudo-dynamic source characterization to include effects of fault roughness that represents small-scale geometrical variations of the rupture surface with respect to a mathematically idealized plane. We conduct a suite of dynamic earthquake simulations for various rough-fault realizations and analyze their kinematic rupture behavior and radiated seismic wavefield. We examine correlations between the kinematic rupture source parameters to develop a more realistic pseudo-dynamic source representation for ground-motion simulations. Fault roughness leads to two effects that arise due to the fault's non-planarity, namely variations in the out-of-plane position of local moment rate functions (e.g., perturbation in source location), and perturbations in moment tensor orientation. We investigate whether these geometric effects are of importance for near-fault ground motions. We find that the moment tensor orientation needs to be preserved, while the out-of-plane position is of secondary importance. This leads to an effective geometric simplification for specifying the kinematic rupture, in which variably oriented moment tensor sources are imposed on a planar fault, that accurately reproduces the seismic waves of the full rough-fault dynamic rupture. In combination with improved source parameter correlations, we propose an innovative pseudo-dynamic rupture modeling approach that generates realistic rupture scenarios and broadband near-fault ground motions for seismic hazard quantification.

2. *Methods and Parameterizations*

In this section, we briefly outline the numerical modeling approach we deploy to conduct dynamic rupture simulations and describe our rough-fault parameterization. We use a second-order (in space and time) generalized finite-difference method that allows for complex fault geometries through a support-operator method and stretched grids that are mapped onto a computational coordinate system (Ely et al. 2008, 2009). This so-called SORD-code also naturally handles 3D Earth structure. Grid spacing and time stepping are set to ensure numerical stability (Ely et al. 2008), according to the chosen Earth model. Because we want to isolate source effects from wavefield intricacies (i.e., due to scattering in 3D Earth structure), we assume a linear-elastic uniform velocity-density Earth model with $V_p = 6000$ m/s, $V_s = 3464$ m/s, and $\rho = 2700$ kg/m^3. Taking 12 points per minimum wavelength as a nominal requirement to adequately resolve the seismic wavefield for a spatial discretization of d$x = 50$ m, the maximum reliable frequency is $f_{max} \sim 5.75$ Hz. The computational time step is d$t = 0.004$ s. The computational domain spans 150 km $\times$ 120 km $\times$ 30 km, with a pre-specified fault plane of 30 km $\times$ 15 km. We note that the dynamic rupture may not propagate over the entire

fault plane, because roughness, friction, and stress conditions may lead to early rupture arrest. We target $M \sim 7$ scenarios of strike-slip earthquakes on an essentially vertical fault plane, satisfying common source scaling relations (e.g., Mai and Beroza 2000; Leonard 2010). Virtual seismic stations are placed at a regular interval of $h = 2$ km (Fig. 1) at the Earth surface to extract the three components of ground motion from which we then compute near-fault shaking parameters.

For the dynamic rupture simulations, we assume a linear slip-weakening friction law with friction parameters as follows: static friction coefficient, $\mu_s = 0.677$, dynamic (sliding) friction coefficient, $\mu_d = 0.373$, and slip-weakening distance, $d_c = 0.4$ m. The tectonic background stress tensor is chosen homogenous with $\sigma_{xx} = \sigma_{yy} = -60$ MPa, $\sigma_{zz} = \sigma_{xz} = \sigma_{yz} = 0$ MPa, and initial shear traction σ_{xy} as listed in Table 1. Homogenous background stress resolved on a complex-geometry fault plane leads to heterogeneous initial stress for rupture. For completeness, we note that fault opening (tensile crack, mode I) is not allowed in our simulations. Furthermore, to minimize effects due to the artificial initiation by an overstressed asperity, the hypocenter

locations (with respect to the roughness) were chosen to be in areas which are close to failure. For linear slip-weakening and fully elastic medium, very large slip rates may occur, in particular close to the free surface. To minimize this effect, we linearly increase the cohesion in the upper 4 km, reaching 2.4 MPa at the Earth's surface.

We consider three rough-fault realizations, scaled by two different values that define the "height" above the planar fault surface. By means of shifting the roughness pattern periodically, but keeping the same relative position of the hypocenter with respect to the roughness, we are able to efficiently generate many rupture scenarios. To also investigate the effects of the choice of the hypocenter position on the dynamic rupture process (and resulting ground motions), we vary the nucleation point to be in the left, in the center, or in the right of the fault plane (Table 1). Following Galis et al. (2015), we use fixed dimension of the nucleation patch and increase overstress until successful initiation. Initial tractions (constant in the domain) and the stress perturbation in the rupture-initiation zone are selected to ensure rupture nucleation and propagation. In total, we investigate 21 rough-fault dynamic rupture simulations (Table 1).

To parameterize fault roughness in terms of out-of-plane fault geometry, we generate fault-surface realizations as random band-limited two-dimensional surfaces (based on Pardo-Iguzquiza and Chica-Olmo 1993) in which roughness is quantified using the power spectral density of the von Karman correlation function. Correlation lengths a_x, a_z are chosen to be 3 km, and the Hurst exponent is chosen as $H = 1$. This choice of $H = 1$ generates a high-wave number fall-off of the power spectral density consistent with previous studies that assume self-similar fractal surfaces (Dunham et al. 2011; Shi and Day 2013). As discussed further by Shi and Day (2013), this is reasonably consistent with observations, especially over the limited bandwidth of our simulations, though such observations are better fit by self-affine fractal surfaces having smaller H (Candela et al. 2012). The amplitude variations are then scaled according to the ratio of the RMS (root-mean-square of fault roughness) to the along-strike source dimension L_x, taking on values of 0.005 and 0.0075. This approach is similar to the method of Dunham et al. (2011) who
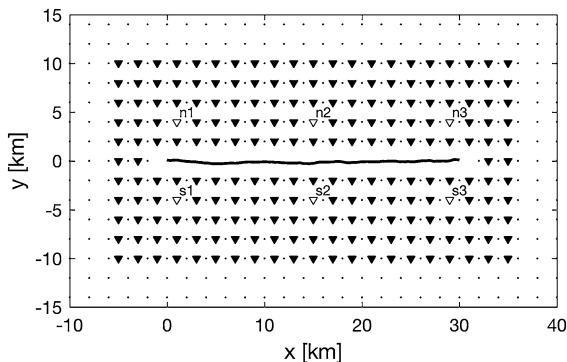

Figure 1
Map view of the fault and receiver geometry for rough-fault dynamic rupture simulations. The nominal fault plane is essentially vertical, the *black* undulating line marks the surface projection of the rough-fault realization for simulation case A1. Epicenters are located toward the left and right edge of the fault, and in the center (see Table 1). The *triangles* indicate virtual stations used to study kinematic representations of rough faults (the locations depicted by *white triangles* are used to compare waveforms, Fourier-amplitude spectra and response-spectral characteristics in subsequent figures) and the *dots* represent the dense grid of virtual stations used for ground-motion analysis

Table 1

Model parameters for the rough-fault simulations

Model	RMS/L	Realization (rand. seed)	HC location	σ_{xy}, Initial shear traction (MPa)	Initiation perturbation (MPa)	M_w
A1	0.005	87	Left	29.38	5.8	6.87
A2	0.005	87	Center	29.38	5.8	6.89
A3	0.005	87	Right	29.38	5.8	6.87
B1	0.0075	87	Left	31[a]	5.8	6.83
B1b	0.0075	87	Left	32[a]	5.8	6.87
B2	0.0075	87	Center	31[a]	5.8	6.85
B3	0.0075	87	Right	31[a]	5.8	6.83
C1	0.005	29	Left	29.38	7.5	6.87
C1b	0.005	29	Left	29.38	6.5	6.87
C2	0.005	29	Center	29.38	7.5	6.9
C3	0.005	29	Right	29.38	7.5	6.87
D1i	0.0075	29	Left[a]	31.5[a]	3.075	6.84
D2i	0.0075	29	Center[a]	31.5[a]	3.075	6.87
D2	0.0075	29	Center	31.5[a]	3.075	6.87
D3i	0.0075	29	Right[a]	31.5[a]	3.075	6.84
E1	0.005	404	Left	29.38	7.15	6.88
E2	0.005	404	Center	29.38	7.15	6.89
E3i	0.005	404	Right	31[a]	5.05	6.95
F1	0.0075	404	Left	31[a]	2.5	6.82
F2	0.0075	404	Center	31[a]	2.5	6.82
F3i	0.0075	404	Right	32[a]	4.25	6.87

We consider three rough-fault realizations (that is, three different random seed values), two values for defining the "height" above the planar fault surface (i.e., two RMS/L values), and three hypocenter locations. Initial tractions (constant in the domain) and the stress perturbation in the rupture-initiation zone are selected to ensure rupture nucleation and propagation. Entries marked by a letter (a) deviate slightly from the targeted value to ensure successful initiation and rupture propagation. In total, we investigate 21 rough-fault dynamic rupture simulations

specify fault roughness using the amplitude-to-wavelength ratio $\alpha \sim 10^{-2}$. Wavelengths shorter than 500 m (that is 10 grid points) are removed by setting the power spectral density to zero at the respective wave numbers k. This process generates the desired random band-limited fault surfaces that undulate in-and-out of the nominal (mathematical) rupture plane (Fig. 2). Note that despite identical RMS/L value (RMS/L = 0.005) for models A, C, and E, their spatial patterns vary due to different random seed numbers in the random number generator. Models B, D, and F share the spatial pattern with models A, C, and E, respectively, but RMS/L = 0.0075 results in larger roughness amplitudes.

3. Rough-Fault Dynamic Rupture Properties

We now describe key aspects of the dynamic rupture behavior due to different roughness parameterizations and hypocenter locations, as well as the resulting ground-motion characteristics in the near-field. The seismic wavefield is stored for a dense grid of receivers (Fig. 1), but we focus on a few representative locations to discuss waveform and spectral characteristics of synthetic seismogram, while ShakeMap-like displays of the spatial distributions of peak ground velocity (PGV) illustrate the overall near-field characteristics.

3.1. Rupture Dynamics for Different Rough-Fault Parameterizations

To document the rupture complexity generated when considering dynamic ruptures on rough faults, we first display snapshots (at 1-s time intervals) of slip velocity magnitude for model A1 and B1 (Fig. 3). The key observation is that a small change in the roughness amplitude (from RMS/L = 0.005–0.0075) significantly modifies the space–time evolution of the rupture process. For A1, the rupture first propagates predominantly in up/down dip directions (that is, in anti-plane mode) and only later develops a consistent rupture front propagating in along-strike direction (predominantly
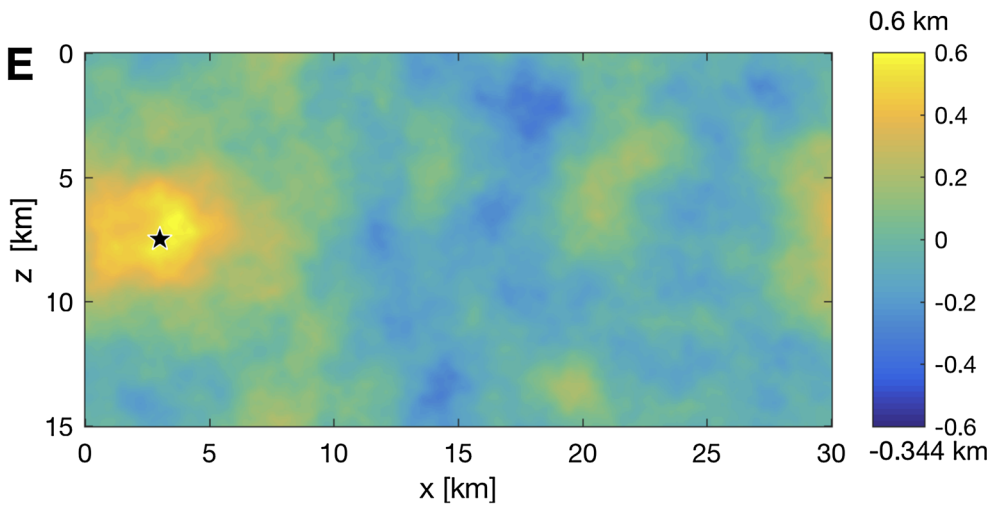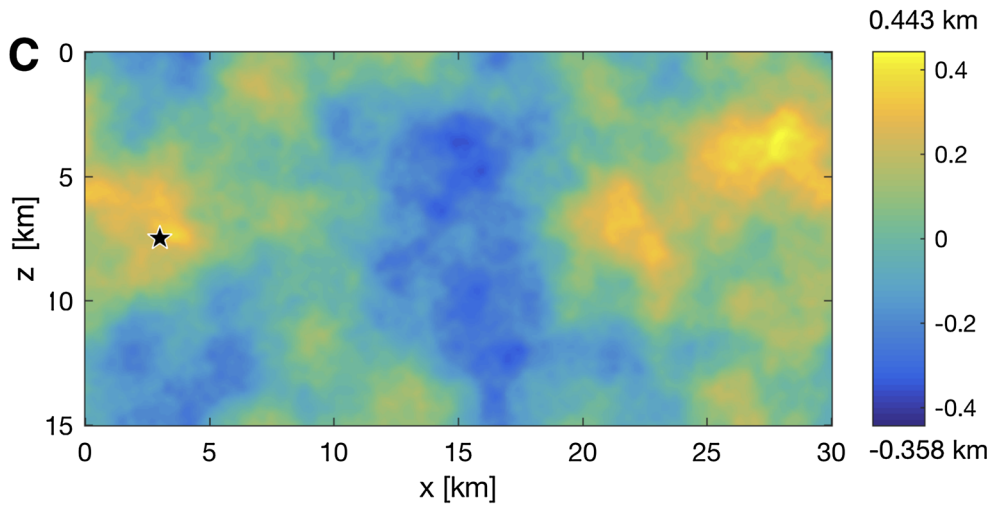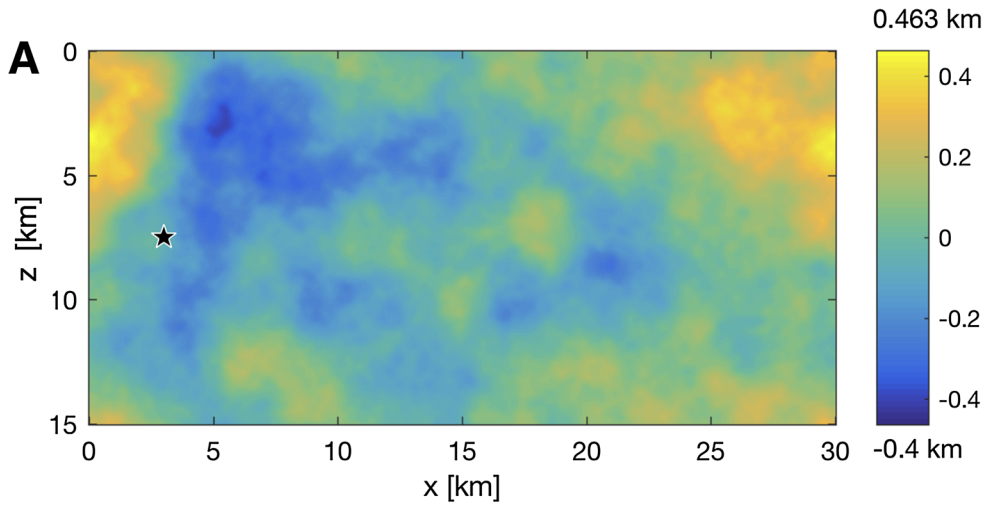
Realizations **A**, **C**, and **E** (see Table 1) of rough-fault rupture surfaces. The *black stars* mark the chosen rupture-initiation points (note that we use fixed position of hypocenter with respect to the roughness). Models **B**, **D**, and **F** share the spatial distribution of roughness with models **A**, **C**, and **E**, respectively, but with higher amplitude (in terms of RMS/L). See text for details and Table 1

in-plane mode). This rupture pattern is in contrast to the typical behavior seen on planar faults, where ruptures tend to propagate faster in in-plane direction and slower in anti-plane direction, leading to elliptical rupture shape. We conjecture that the stronger promotion of the anti-plane mode here is consequence of the critical crack length for anti-plane mode being shorter than for in-plane mode (e.g., Andrews 1976a, b). As can be seen in Fig. 4, low rupture speed and peak slip rates together with more complex rupture shape are characteristic for the first phase. However, as soon as the rupture forms the coherent rupture front, it continues to propagate with only tiny variations in the shape of the rupture front and peak slip rates. In contrast, B1 is characterized by an overall shorter, yet more complex rupture evolution that contains multiply connected rupture fronts and isolated areas in which rupture almost arrests. Remarkable variations of peak slip rate together with a complicated rupture front are observed even after a coherent rupture front is formed. The difference in duration of rupture propagation (~ 18 s for A1 compared with ~ 13 s for B1) is a consequence of the longer initiation phase in A1, and not a consequence of faster rupture propagation in B1. To insure that model B1 propagates over the entire fault plane, its initial background shear stress was raised to 31 MPa, compared to model A1 in which the initial shear stress was 29.38 MPa. Interestingly, the complex rupture pattern does not manifest itself in a complex spatial distribution of final slip; consequently, the final slip of A1 and B1 are remarkably similar (Fig. 4).

Figure 4a–f provides simple summary plots of the kinematic source parameters final slip, peak slip rate, rupture speed, and moment rate function for simulations A1, B1, C1, D1i, E1, and F1 (Table 1), with the hypocenter at the left edge of the fault. Ruptures that nucleate close to the fault edges tend to propagate as rupture pulses, whereas ruptures initiated in the fault

center (A2, B2, C2, D2, D2i, E2, and F2; not shown) reveal a more crack-like propagation. Consistent with our model setup, the final moment magnitudes, M_w, fall in the range 6.8–7 (Table 1). We note that rougher faults (RMS/L = 0.0075) tend to produce somewhat smaller magnitudes than less rough faults (RMS/L = 0.005), indicated by average magnitudes of M_w 6.84 and M_w 6.89, respectively. Ignoring the region of forced rupture, rupture propagation appears overall smooth for RMS/L = 0.005 (models A, C, E), with near-constant rupture speed V_r = 2.0–2.5 km/s. However, these ruptures tend to slow down in regions of steep restraining slopes due to the roughness (i.e., slopes with increased initial normal traction due background stress and orientation of the slope) before being able to propagate over these geometrical obstacles. Similarly, rupture speed tends to be higher in regions with releasing slopes (i.e., slopes at which normal traction is reduced). In contrast, if roughness is stronger (RMS/L = 0.0075), the rupture front is much more complicated, often multiply connected, showing isolated patches of almost arrested rupture or strong localized rupture acceleration. Locally, rupture speed V_r exceeds the shear wave speed, but extended regions of super-shear ruptures are absent. These localized zones ("islands") of V_r reaching the P wave speed indicate strong small-scale heterogeneity that will affect high-frequency seismic radiation. These islands correspond to either asperities, which are triggered by stress changes induced by propagating waves, or barriers, which break after the main rupture front passes by.

We observe that peak slip rate distributions on the fault are smoother than those of rupture velocity. Peak slip rates are mostly in the range of 2–5 m/s, occasionally exceeding 5 m/s locally (e.g., A1, close the surface). We expect that using a rate-and-state friction law with velocity strengthening at shallow depths and/or including plasticity in the simulations (e.g., Dunham et al. 2011; Shi and Day 2013) would limit the slip rates, as proposed by Andrews (2005). On the other hand, the localized high slip rates have only marginal effects on the radiated wavefield, as shown in a separate simulation discussed below. Peak slip rate tends to be lower in regions of restraining slopes; however, it varies significantly in regions of releasing slopes, suggesting that peak slip rate is highly sensitive to the local breakdown conditions at
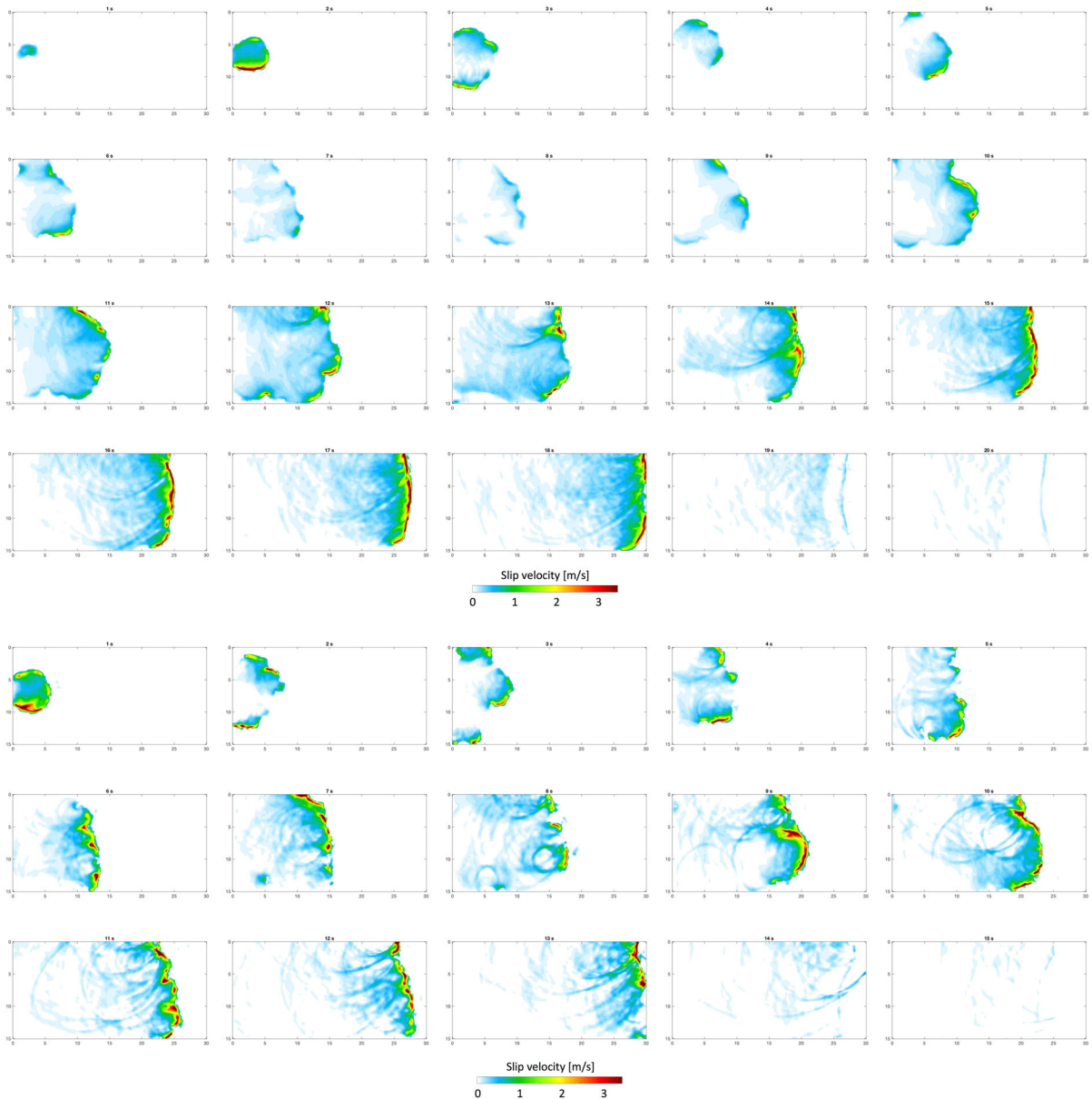
Figure 3

Snapshots (at 1-s time interval) of dynamic rupture simulation on rough faults for cases *A1* (*top*) and *B1* (*bottom*) (see also Table 1). The series of snapshots captures differences in rupture propagation due to small variation of fault roughness. For A1, rupture propagation is first characterized by a slow rupture speed and low peak slip rates, followed by a formation of a coherent rupture front with higher peak slip rates. In contrast, for *B1*, we observe much more complex rupture with multiple rupture fronts and significant variations of peak slip rate

the crack tip, rather than to the underlying fault roughness.

Complex rupture behavior can also be identified from the total moment rate functions that often show 2 or 3 peaks, indicating different rupture episodes

(Fig. 4). Multiple peaks may occur for different reasons. For example, for model A1 the rupture first phase is characterized by small moment release; only after the formation of a coherent rupture front (at ∼ 10 s), the rupture starts radiating more energy. In
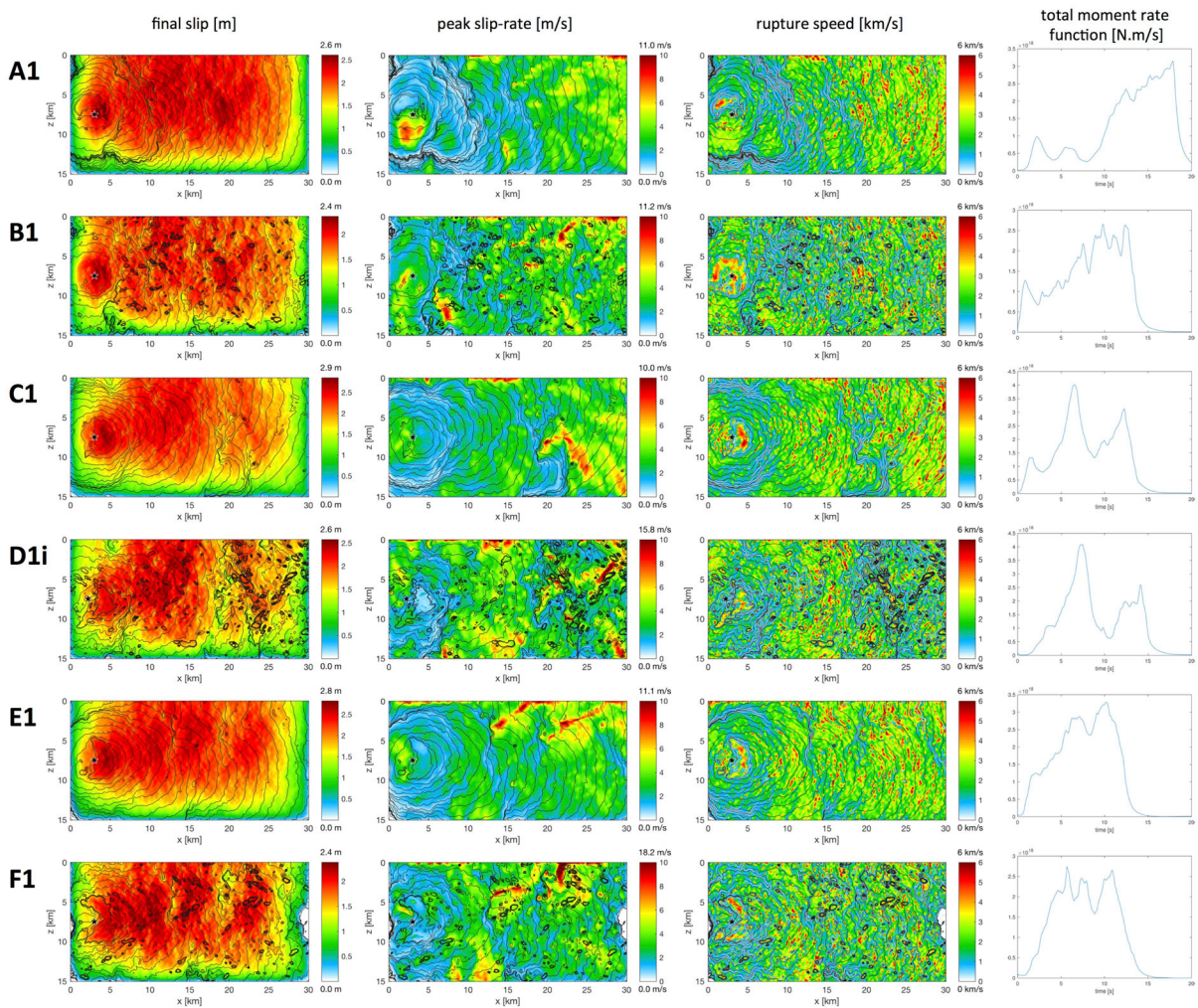
Figure 4

Graphical display of final slip (first column, in meters), peak slip rate (second column, in m/s), rupture speed (third column, in km/s), and the total moment rate function (fourth column, Nm/s) for six rough-fault dynamic rupture scenarios with nucleation at the left edge of the fault (indicated by the *black star* see Table 1). Contour lines in the first, second, and third columns depict the rupture front at 1-s intervals. *A1*, *C1*, and *E1* share the same roughness value (RMS/L = 0.005), likewise *B1*, *D1i*, and *F1* (RMS/L = 0.0075), but different random seed values hence different roughness patterns. Roughness patterns for *A1* and *B1*, *C1*, and *D1i*, as well as *E1* and *F1* are created with the same random seed values

contrast, in model D1i the initiation phase is very short and rupture propagates relatively soon (corresponding to the first peak in moment rate). However, then the rupture hits a barrier and is almost arrested (local minimum in moment rate at ∼ 10 s). Eventually, rupture breaks the barrier and continues to propagate, leading to the second peak in moment rate function. Rupture scenarios with hypocenter in the center of the fault plane display simpler moment rate

functions with almost triangular shape, owing to the bilateral rupture propagation.

Maximum fault slip reaches ∼ 3 m for scenarios with hypocenters close to the fault edge. On a larger scale, the slip distribution is relatively uniform, akin to slip distribution from ruptures on planar uniform faults. Overlain over the large-scale slip pattern, the ruptures show small-scale slip variations that resemble the underlying fault roughness pattern. More
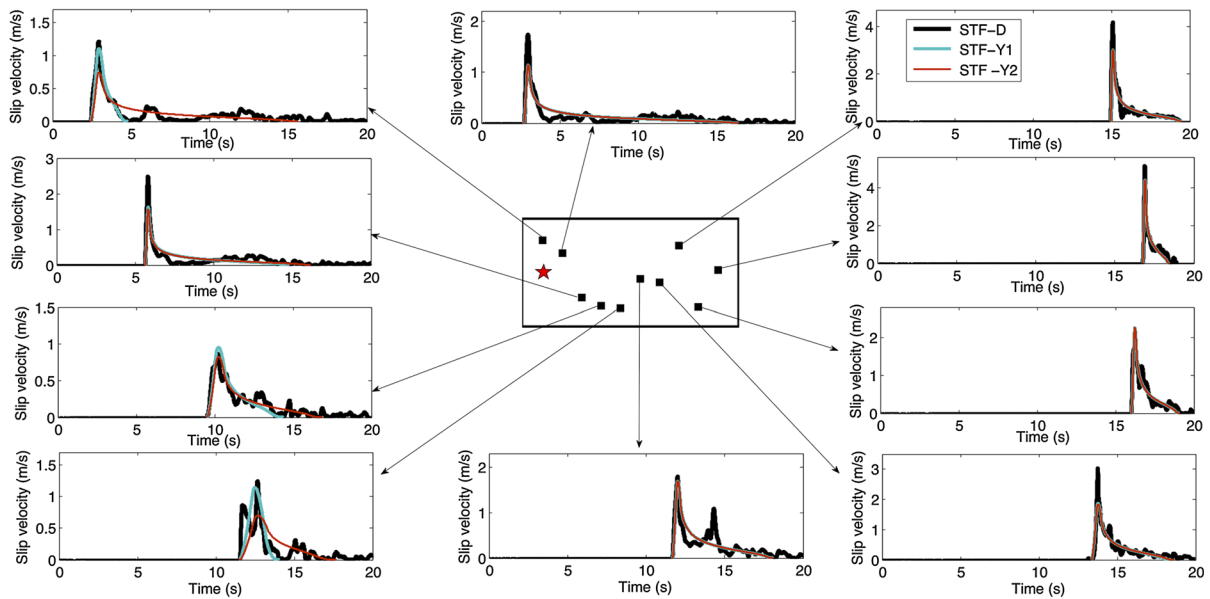
Figure 5

Examples of source-time function (STF-D) from dynamic rupture model A1 given in *black* overlaid with two alternative fits of the regularized Yoffe function (Tinti et al. 2005), STF-Y1 and STF-Y2. The *plot* in the center shows the corresponding points on the fault geometry. The two kinematic approximations of the dynamic source-time function (STF-D) become increasingly similar with distance from hypocenter

precisely, slip tends to be higher or lower in regions of releasing or restraining slopes, respectively. For models with hypocenter in the center, the slip distribution has a clear maximum in the hypocentral region, with maximum slip reaching ∼ 3.5 m. Although the heterogeneity of the final slip map seems to resemble the underlying fault roughness pattern, individual large asperities (aside from the nucleation region) are not present. However, localized high-slip patches (i.e., slip asperities) are expected from earthquake source inversion studies that provide evidence for the complexity of fault slip and the concentration of seismic moment release within limited fault regions (e.g., Hartzell and Heaton 1983; Ide 2007; Mai and Beroza 2002; Mai and Thingbaijam 2014; Thingbaijam and Mai 2016). We hypothesize that to obtain realistic multi-scale slip heterogeneity a combination of stress heterogeneity (related to large-scale slip heterogeneity) and fault roughness (relevant for short-scale slip heterogeneity) is needed. Stress heterogeneity will also arise from past slip events on rough faults.

3.2. Parameterizing the Dynamic Source-Time Function

Let us now examine the local slip rate functions. Representative examples are shown in Fig. 5 for model A1. Their overall shape follows the Yoffe-type source-time function (e.g., Tinti et al. 2005), but reveals important local variations in terms of secondary peaks, elongated tails, and a very energetic onset.

The complexity of the dynamic source-time functions (henceforth referred to as STF-D) reflects the space–time variability of the rupture process and is a source of high-frequency seismic radiation. Standard source-time functions used in kinematic ground-motion simulations (boxcar, triangle, cosine) fall short in reproducing these characteristics. Here, we use the regularized Yoffe function (Tinti et al. 2005) as a kinematic representation of the dynamic STF (henceforth STD-Y) to facilitate our statistical modeling. For each point on the fault, we extract the STF-Y by applying a temporal window based on criteria for rupture onset and rupture arrest,

summarized below, and then estimate the corresponding kinematic source parameters for this STF-Y.

In fitting the regularized Yoffe function, we consider two constraints to define rupture arrest, while rupture onset is identified when slip velocity first exceeds 0.001 m/s prior to reaching the peak slip velocity. To define rupture arrest, our first STF approximation (STF-Y1) is obtained by limiting the time window to the duration of slip until slip velocity first falls below 0.001 m/s following the peak slip velocity. We propose a second alternative, STF-Y2, based on the constraint that at least 95% of the total (dynamic) slip is retained. STF-Y1 is hence slip rate constrained, while STF-Y2 also slip-preserving. In each case, the fitting is achieved by a grid search over the model parameters.

Figure 5 presents examples of STF-Y1 and STF-Y2 for selected points of model A1. Complicated STFs that exhibit multiple slip episodes are reproduced by Yoffe functions that appear as skewed triangle STFs or even a cosine-type STFs. In contrast, peaked dynamic STF appears as Yoffe functions with a short rise toward the peak slip rate. This behavior has been described also by Tinti et al. (2005) who define the duration of the initial rise as the acceleration time, Tacc.

Computing the total moment rate function from the fitted Yoffe-like STFs for model A1, we find that STF-Y1 retains $\sim 86\%$ of the total seismic moment of the dynamic rupture, while it is $\sim 97\%$ when using STF-Y2; in both cases, the shape of the moment rate function is well preserved (Figure S1). Consequently, we adopt the second approximation to generate simplified kinematic rupture models for further analysis. To better understand the effects of the two STF approximations on the overall kinematic source parameters, and subsequently the resulting ground motions, we compare the statistics of the kinematic parameters given by the different versions of the STF-Y with respect to those given by the STF-D (Figure S2). While the spatial distribution of slip and its statistical one-point distribution are well preserved for STF-Y2, we find that the one-point statistics (i.e., the histograms) of peak slip rate are more strongly affected. Applying the Yoffe function regularization retains the spatial structure of the peak slip rate

distribution, but filters very high values. We remark that this in fact is a desired consequence of the kinematic rupture model approximation, as it partially mimics the effects that velocity strengthening or plasticity would have on the dynamic rupture process, leading to a strong slip rate reduction (e.g., Andrews 2005; Gabriel et al. 2013).

4. Ground Motions for Simplified Kinematic Rupture Models

Our goal is to develop a pseudo-dynamic source characterization that encapsulates the effects of rupture dynamics on rough faults into an effective kinematic rupture representation that replicates the near-field ground motions. We examine how the certain geometrical features of rough faults can be simplified, and how this simplification affects the seismic radiation. We also quantify how simplifying the dynamic source-time function (STF-D) to an effective kinematic representation (STF-Y1 or STF-Y2) changes ground-motion characteristics. Kaeser and Gallovic (2008) examined effects of non-planar kinematic earthquake ruptures on near-field ground motions by comparing to their equivalent planar ones. They find that geometrical irregularities lead to increased high-frequency radiation, while some effects on lower frequencies are observed as well. They show that correctly incorporating local strike and dip variations of the rupture surface is important for near-source shaking simulations. However, their work is based entirely on pre-specified kinematic rupture models, and thus, dynamic rupture effects due fault-surface complexities are not represented.

To examine the effects of local strike, dip, and rake, as well as the off-fault position of the slip rate (moment rate) function, we define four additional geometrical configurations (Fig. 6). These four geometrical parameterizations, denoted "full," "topo," "flat," and "plan," are defined as follows: (a) "full" contains the full roughness information (off-fault position, strike, dip, and rake) of the local slip vector; (b) "topo" retains the off-fault position (distance from the planar fault), but strike, rake, and dip are fixed to the corresponding values for the average plane and slip vector direction; (c) "flat" is a planar
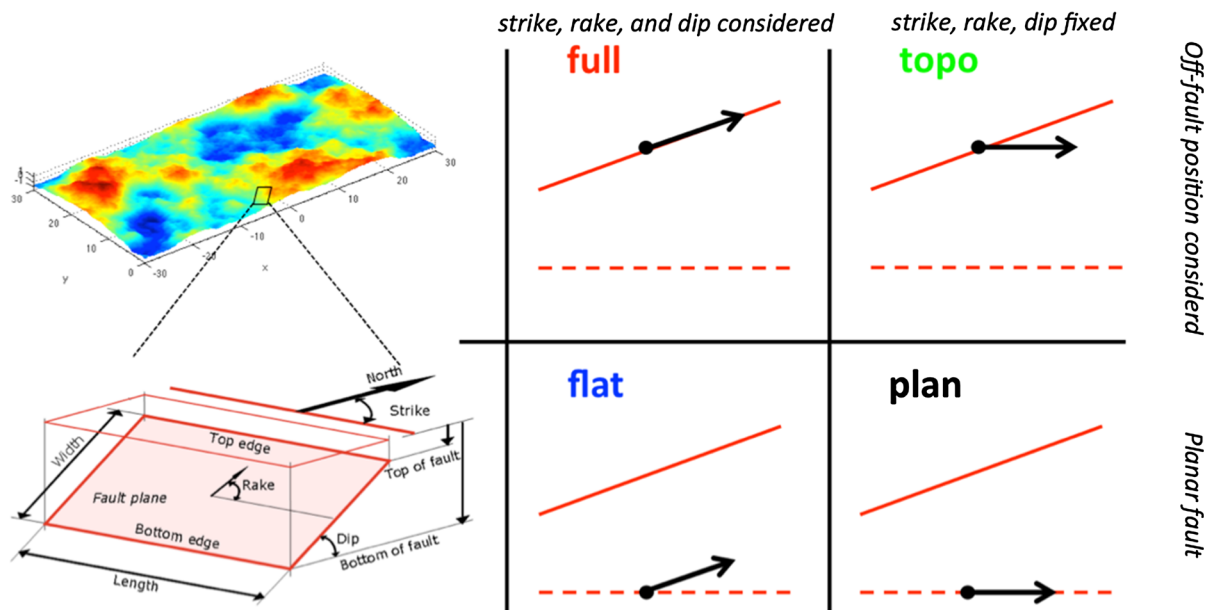
Figure 6

Conceptual figure to illustrate our nomenclature to describe the rough-fault moment tensor position and orientation. *Top-left* shows an example rough-fault realization in which each individual patch can be described by the standard strike–dip–rake definition of the slip vector (*bottom left*). The matrix to the right graphically indicates the use of the roughness information: "full" considers the off-fault position as well as strike, rake, and dip of local slip vector; "topo" considers only its topographic position (off-fault position accounted for; strike, rake, and dip fixed); "flat" considers a flattened representation (off-fault position ignored; strike, rake, and dip of moment tensor accounted for); "plan" uses the simplest planar representation (off-fault position ignored; strike, rake, and dip of moment tensor fixed)

fault representation (off-fault position ignored), but strike, rake, and dip of the local moment tensor are respected; and (d) "plan" is the simplest planar representation in which the off-fault position is ignored, and strike, rake, and dip of moment tensor are fixed as for "topo."

To illustrate how fault roughness affects the local moment tensor orientation, Fig. 7 shows spatial on-fault distributions of strike, dip, and rake for models A1 and B1, together with the probability density functions for A1 and B1, as well as for all 21 models (Table 1). Because strike and dip are determined solely by fault roughness, their almost perfect normal distributions are related to the one-point statistics of the normally distributed random fields of roughness. On the other hand, the local slip direction (rake angle) is a result of the dynamic simulations and reveals strong heterogeneity in the spatial rake distributions.

To create the complete geometrical description of a kinematic source, the distributions of strike, dip, and rake angles are needed. Strike and dip can be computed directly for a given/chosen fault roughness. However, the rake angles are determined by the dynamic rupture process and hence need to be derived from other source quantities. Figure 7 reveals pronounced anti-correlation between the spatial distributions of rake and dip, which is further illustrated in Figure S3. We therefore propose to approximate the spatial distribution of rake based on the normalized low-pass-filtered variations in dip, as $\lambda(x, y) = -C[\delta(x, y - \bar{\delta})]$, where $\lambda(x, y)$ is the approximated rake, $\delta(x, y)$ is the low-pass-filtered dip angle distribution, and $\bar{\delta}$ is the average fault dip (90° in this case). The negative sign denotes the anti-correlation, and C is a normalizing constant computed from the condition to preserve the standard deviation (σ) of the dip angle, that is $C = \sigma(\delta)/\sigma(\lambda)$. Through trial-and-error, we determine that a Gaussian filter with a standard deviation of 500 m and corresponding filter width of 2000 m provides an adequate approximation (Fig. 7, bottom row).
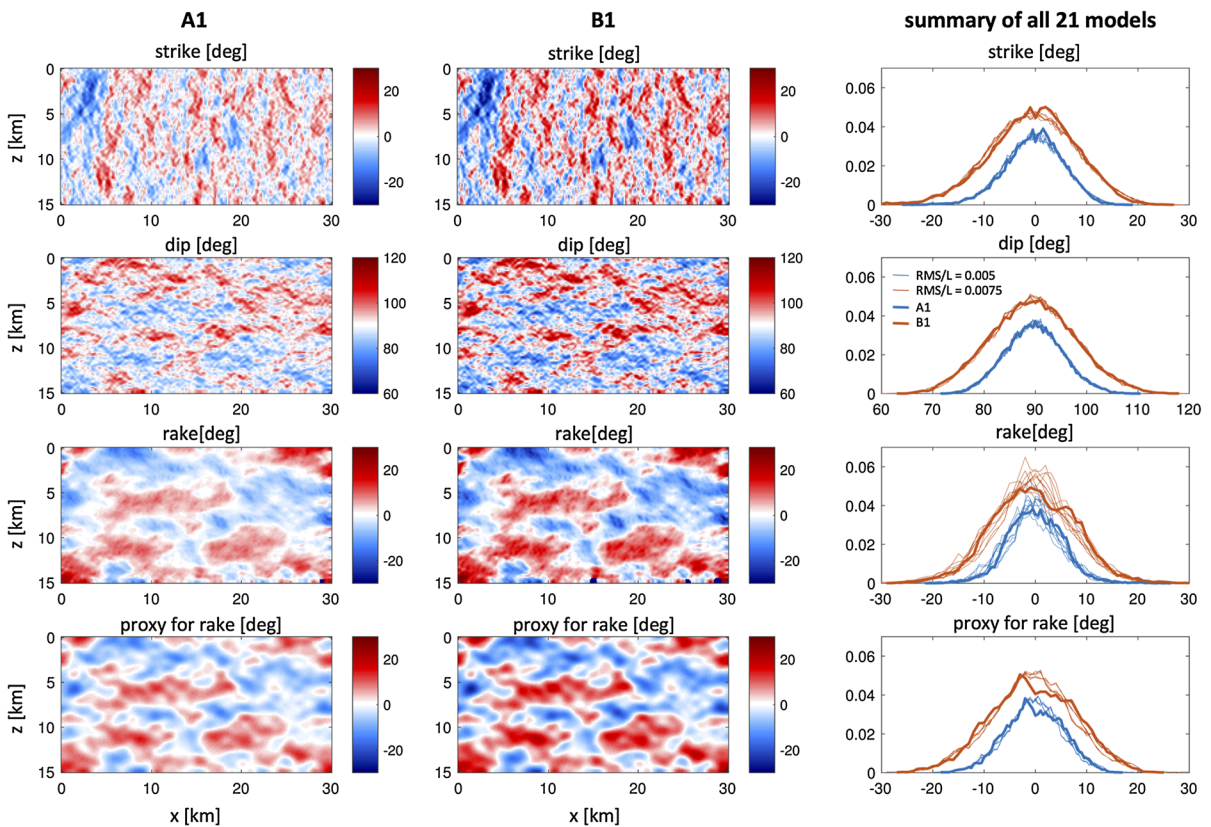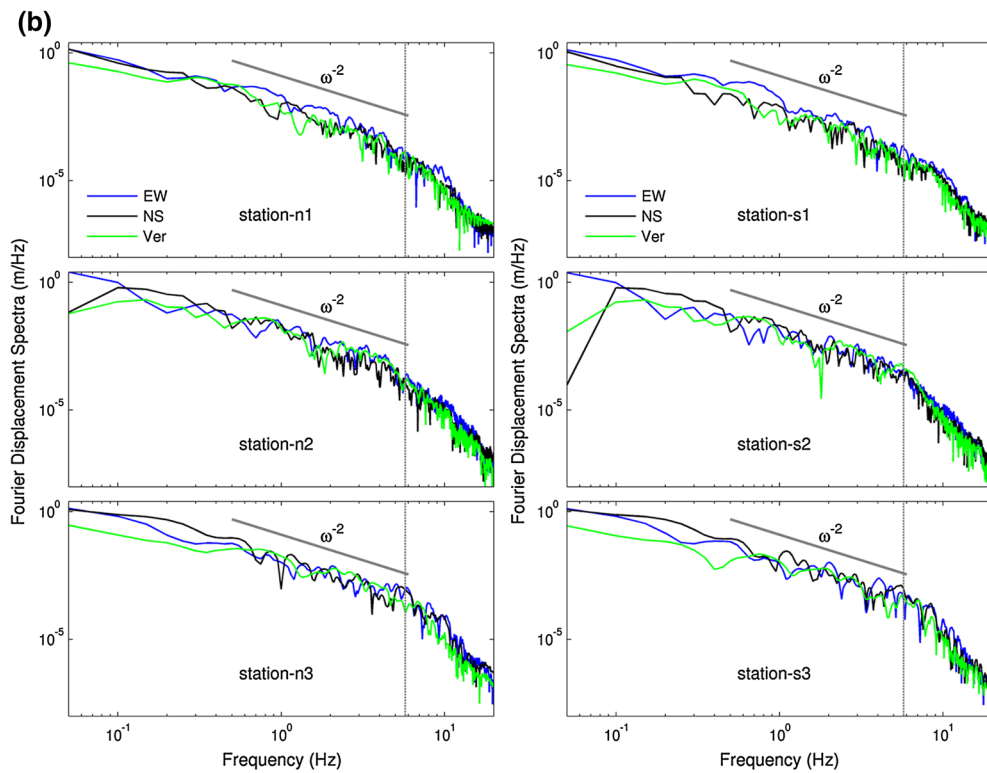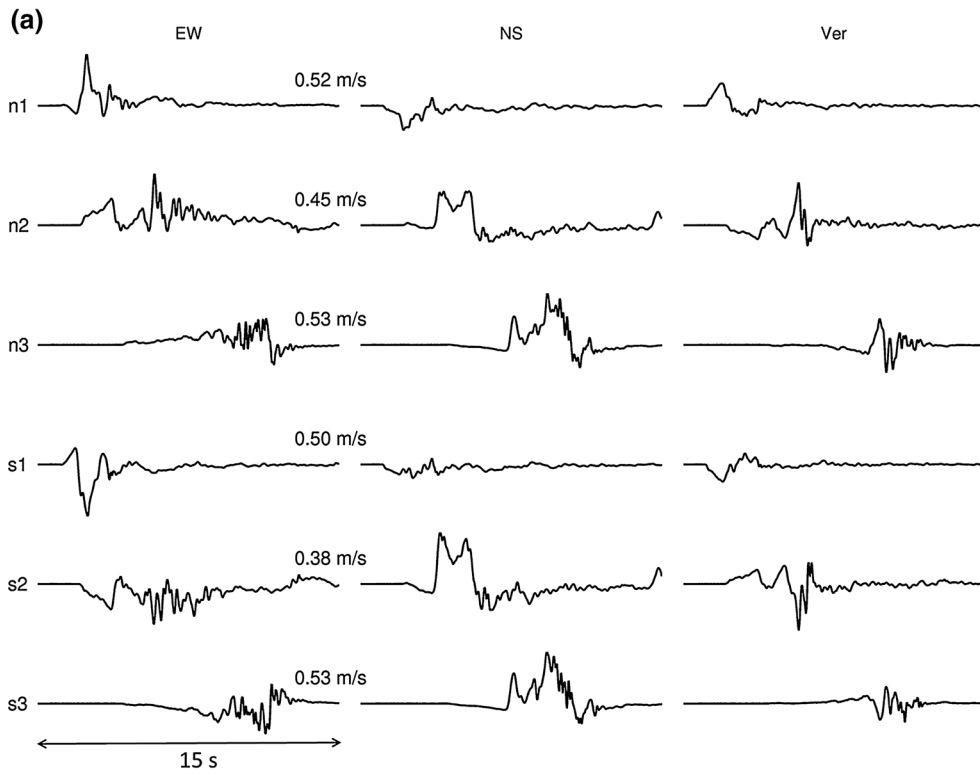
Figure 7

Distributions of strike, dip, rake, and approximated rake (*top* to *bottom panels*), for model *A1* (*left*), *B1* (*center*) and corresponding summarizing probability density functions for all 21 models (*right*). The proxy for rake captures the same spatial pattern as the original rake resulting from the dynamic simulations, but avoids reproducing small-scale variations. The *blue* and *red curves* in the *right panels* depict the PDFs for the rake angles for models with roughness realizations of RMS/L = 0.005 and RMS/L = 0.0075, respectively. For comparison, the corresponding PDFs for model *A1* (*left column*) and *B1* (*center column*) are overlain as *bold lines*

Next, we conduct kinematic ground-motion simulations for simplified geometrical representations; later in this study, we also consider the regularized Yoffe functions STF-Y1 and STF-Y2. These are compared to the complete dynamic rupture simulations to examine the differences in resulting seismic waveforms, their Fourier amplitude and response spectral characteristics, and near-source ShakeMaps of peak ground velocity (PGV). For the purpose of this study, the kinematic rupture representation in our numerical simulations maps the moment density into a finite set of point sources. This source representation is therefore not smooth at the scale of the mesh, and the computed seismic wavefield only becomes accurate a few mesh points away from the fault. Correspondingly, we exclude receiver locations less

than 1 km (or 20 grid points) away from the fault surface projection in our ground-motion analysis.

4.1. Ground-Motion Characteristics for Simplified Geometrical Representations

Here, we investigate the effects of moment tensor orientations and off-fault position on the resulting seismic wavefield from dynamic model A1 and its corresponding four kinematic models A1-full, A1-flat, A1-topo, and A1-plan. In these kinematic models, the dynamic source-time functions (STF-D's) are used and mapped onto the simplified geometric fault representations. To illustrate the richness in waveform complexity due to the rough-fault dynamic simulations, we plot in Figs. 8 and 9

◄Figure 8

Velocity waveforms and Fourier amplitude spectra (of displacements) for three components at six different stations (s1–s3, n1–n3, Fig. 1) for dynamic model A1. Particle velocities (in m/s) are normalized by the maximum absolute amplitude of the three components at each station. The displacement spectra depict ω^{-2}-decay high-frequency decay (*gray solid line*) up to the nominal highest resolved frequency ($f \sim 5.75$ Hz; marked by *gray dashed line*)

velocity and acceleration synthetics, respectively, at six near-field location (s1–s3, n1–n3, Fig. 1) and corresponding Fourier amplitude spectra. We recall that the highest resolved frequency is $f_{max} \sim 5.75$ Hz. A corresponding analysis using pseudo-spectral acceleration (PSA) is provided in Figure S4 of the Electronic Supplement.

Figure 10 then displays synthetic seismograms at the same six sites for five parameterizations of model A1: the original dynamic simulation and then by injecting the local dynamic slip rate functions (STF-Ds) into kinematic simulations using the geometric definitions of Fig. 6. Notice the striking waveform similarity (ground velocity, in m/s), for all three components on all six stations. The visual comparison shows that all four kinematic sources accurately reproduce the full dynamic simulation. While this is expected if the complete moment tensor orientation and off-fault position is retained (case A1-full), the waveforms appear also almost identical for the geometric approximations "topo," "flat," and "plan." We also find that not only the waveforms are very well reproduced by the approximation "flat," but also that the Fourier amplitude spectra in displacement (Figure S5) and acceleration (Figure S6) exhibit identical shapes following the ω^{-2} model up to the maximum resolved frequency. Similar results are obtained for the rougher case B1 comparing ShakeMaps and waveforms (Figure S7), indicating that this is not a case-specific finding, but a general feature.

However, subtle differences exist in waveform shapes and amplitudes, as demonstrated by PGV ShakeMaps (Fig. 11, showing GMRotD50—the orientation-independent peak ground velocities defined by Boore et al. 2006—for the two horizontals components). To further quantify the differences in waveforms, we examine the wavefield at 214 stations

and calculate the absolute maximum of the cross-correlations coefficient (C1 in Eq. 1) between the dynamic and kinematic velocity waveforms, at all stations and for each component. We also evaluate as the absolute maximum of autocorrelation (C0) for the dynamic model (Eq. 2), which is essentially the squared L^2 norm of signal for zero time lag.

$$C1 = \max\left(\left|\int f(\tau) - g(t - \tau)\mathrm{d}\tau\right|\right), \quad (1)$$

$$C0 = \max\left(\left|\int g(\tau) - g(t - \tau)\mathrm{d}\tau\right|\right). \quad (2)$$

In Eqs. (1) and (2), $f(\tau)$ and $g(\tau)$ represent the time-dependent velocity waveforms of the kinematic and dynamic models, respectively. Both $C0$ and $C1$ are normalized to maximum values of unity. We then quantify the relative error (RE) for station i and component j as

$$\mathrm{RE}_{ij} = \frac{C1 - C0}{C0}, \quad (3)$$

and the total relative error for both horizontal components as

$$\mathrm{RE}_i = \sqrt{\mathrm{RE}_{EW}^2 + \mathrm{RE}_{NS}^2}. \quad (4)$$

Consequently, the relative error will be zero if waveforms are identical, and near unity if they are very different. We only use horizontal components in Eq. (4) since ground-motion prediction equations largely neglect vertical ground motions. Thus, we chose an error metric consistent with common earthquake engineering practice.

The relative error RE for the four kinematic models with respect to the dynamic rupture model A1 are shown in Fig. 12. We observe smaller errors for A1-full and A1-flat than for A1-topo and A1-plan; differences in RE between A1-full and A1-flat are negligible, except in the extreme forward directivity direction. Small RE values (mean of 2%, max RE $\sim 10\%$) for A1-flat indicate that its wavefield closely replicates the one of the reference dynamic model. Statistics of RE values show mean $\mu = 0.02$ (standard deviation $\sigma = 0.01$) for A1-flat, that is, only a 2% difference in waveforms compared to dynamic model A1. Approximations A1-topo and A1-plan have mean RE values $\mu = 0.04$ ($\sigma = 0.06$)
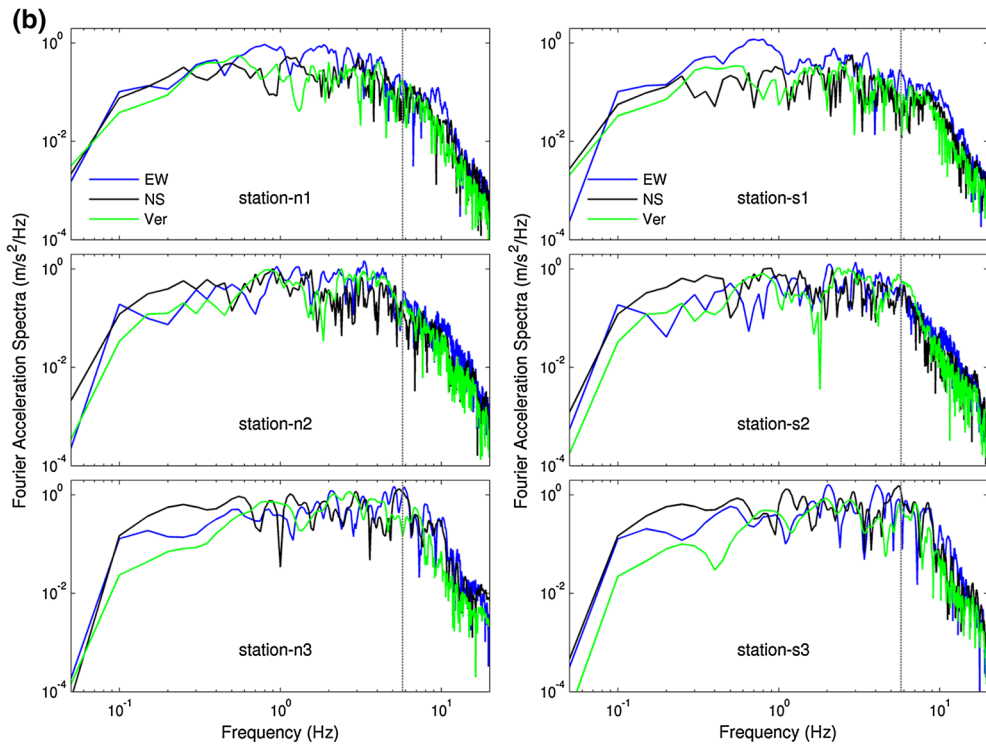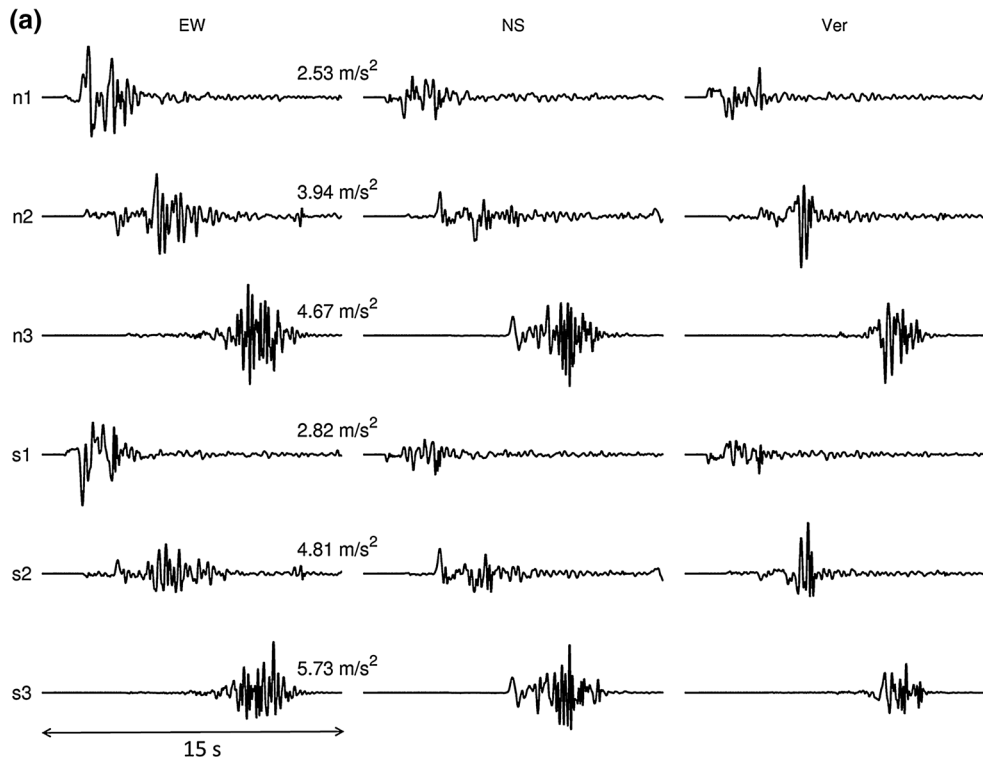
(a)

(b)

and $\mu = 0.06$ ($\sigma = 0.08$), respectively, indicating much larger deviation from the dynamic model. Our analysis of relative errors suggests that moment tensor orientations are of primary importance on near-field ground-motion complexity, while the off-fault position is less important. Therefore, preserving moment tensor orientations only but mapping the rupture model onto a flat (planar) fault appears to be sufficient to reproduce waveforms and shaking levels of rough-fault dynamic ruptures.

We further quantify the ground-motion differences based on model bias MB

$$MB_i = \ln\left(\frac{PGV_{kin}}{PGV_{dyn}}\right), \qquad (5)$$

where PGV_{kin} and PGV_{dyn} are GMRotD50 of ground velocities for the kinematic models (A1-full, A1-flat, A1-topo, or A1-plan) and the dynamic model A1. If $MB = 0$, the shaking levels in terms of PGV are identical; if $MB > 0$, the kinematic model generates higher PGV. The spatial distribution and statistics of model bias for the four kinematic models are shown in Fig. 13. Model bias for A1-full and A1-flat (both preserving the moment tensor orientation) are lower than for A1-topo and A1-plan, but differences between A1-full and A1-flat are more pronounced than between A1-flat and A1-topo or A1-plan. The spatial structure of the model bias for A1-full corre-lates with the directivity effect (Fig. 11), while it appears spatially uncorrelated for the other three cases. Examining the normalized frequency distri-bution of model bias reveals a near-zero mean of MB, but standard deviations that vary from 0.02 to 0.09. Note that a model bias value of 0.2 indicates PGV differences of about 22% (Eq. 5). Therefore, MB standard deviation shows 4% PGV mismatch for A1-flat compared to PGV variations of 7% (or 9%) for A1-topo (A1-plan). These observations are consistent with the above findings based on relative errors.

Next, we test our findings from model A1 with simulations for model B1 (rougher fault topography, Table 1) over a larger domain and for more stations ($N = 3350$), based on relative error RE and model bias MB computed only for the most promising geometric approximation "flat" (Fig. 14). We observe near-zero relative errors in forward and backward rupture direction, but higher values per-pendicular to the fault. The frequency distribution of relative errors is nearly uniform, with mean $\mu = 0.05$ ($\sigma = 0.03$), which is higher than for A1-flat (Fig. 12). Zooming into the narrower region around the fault (black rectangles in Fig. 14) used for analyzing model A1, the corresponding frequency distributions of relative errors and model bias (small inset plots) are more similar to what is observed for A1-flat, albeit the histograms are broader (i.e., have larger standard deviation). The analysis of model B1 confirms our observation that the geometrical approx-imation "flat" for the kinematic source captures the ground-motion signature of the rough-fault dynamic rupture. Hence, local moment tensor orientations are more important for near-source ground motion than off-fault point-source locations. This suggests that to properly account for rough-fault effects in kinematic parameterizations, the off-fault positions of local moment rate tensors can be neglected, while the orientations need to be preserved.

4.2. Kinematic Ground-Motion Characteristics for Variations in Source-Time Function

In the kinematic ground-motion simulations shown above, local dynamic source-time functions, STF-D, were applied to define simplified kinematic rupture models. However, in practice a pseudo-dynamic source model needs to be specified using a parametric source-time function for which the prop-erties of the governing scale or shape parameters can be obtained from independent empirical relations or correlation analysis. We therefore use the previously defined parameterizations of the Yoffe-type source-time function, STF-Y1 and STF-Y2, to define a next class of kinematic source models, applying also the "flat" fault approximation that very well reproduces the seismic wavefield of the dynamic rupture. Further, we test if the simplified proxy rake,
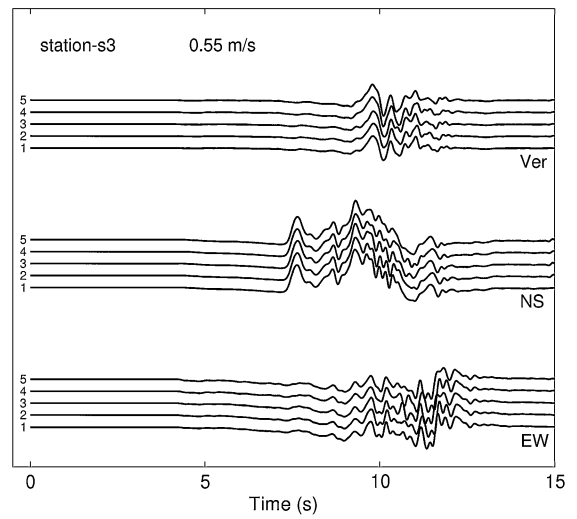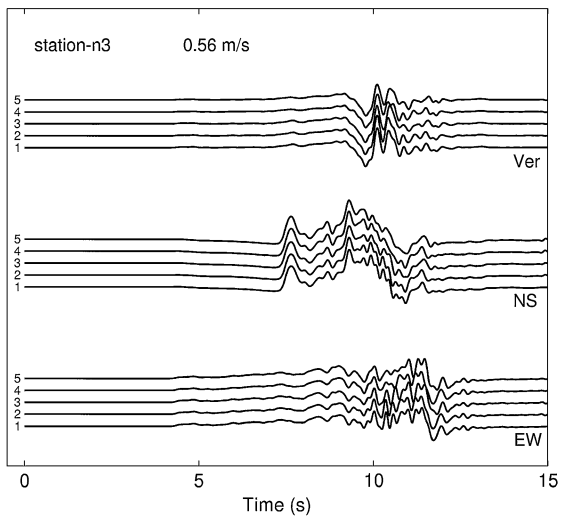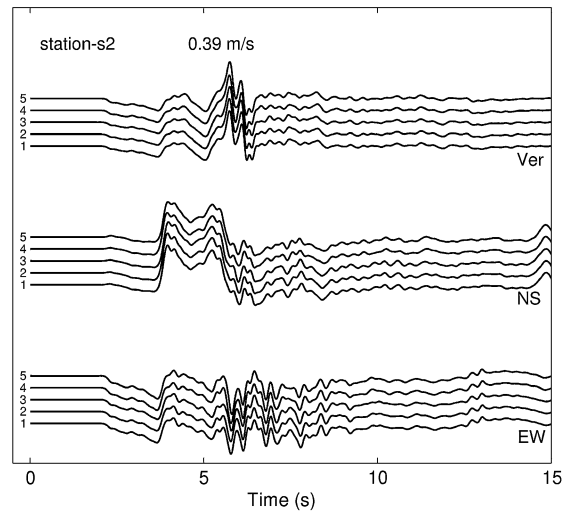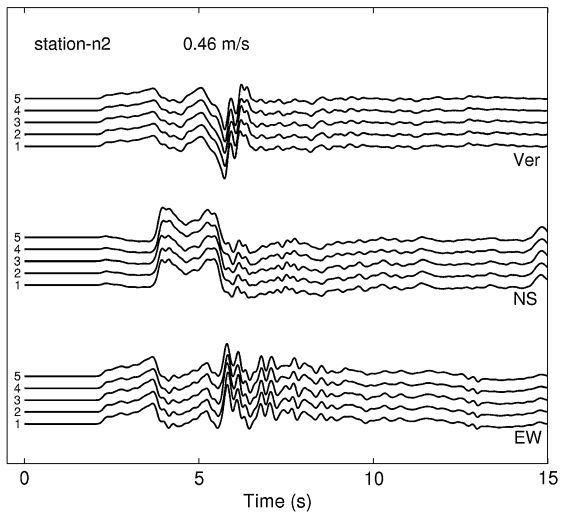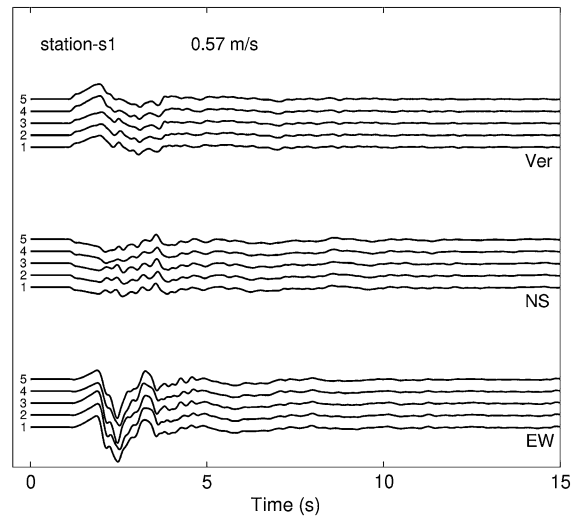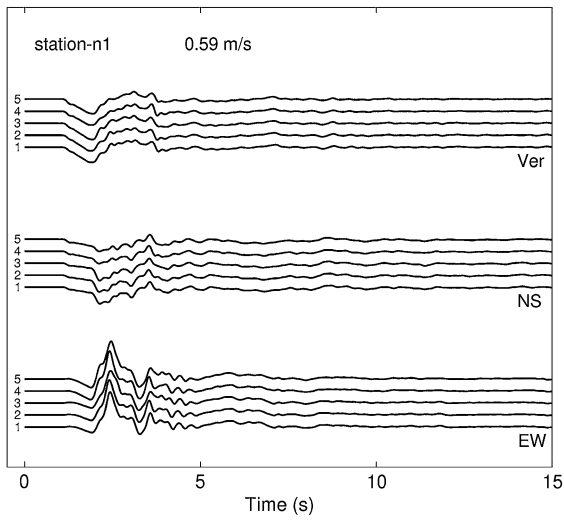
◄Figure 10

Examples of seismograms for the five different rupture characterizations: A1, A1-full, A1-flat, A1-topo, and A1-plan (numbered 1–5, respectively) for three components at six different stations (s1–s3, n1–n3; Fig. 1). Particle velocities (in m/s) are normalized by maximum absolute amplitude of all three components at any given station. Notice that all five simulations provide very similar results, indicating that rough-fault simulations are well reproduced by simplifying the small-scale fault plane complexity according to the geometry approximation in Fig. 6

computed from the dip angle variations of the rough fault (see above and Fig. 7), provides an adequate and readily available parameterization for the local moment tensor orientations.

Figure 15 provides initial insight into the ground-motion reproducibility using further simplification of the dynamic rupture models. PGV ShakeMap comparison of GMRotD50 for the dynamic source and the kinematic models with slip rate constrained (STF-Y1) and slip-preserving source-time functions (STF-Y2) show that the overall ground-motion patterns are very similar. Notice also that PGV statistics even for the 2-km-wide swath around the fault trace are very similar, with PGV values mostly smaller than 1 m/s. However, the highest PGV values for the kinematic rupture are smaller due the smoothing effect of STF-Y1 and STF-Y2 that reduces on-fault peak slip rate values and slightly modifies the slip rate histograms (Figure S2). Further simplification of the kinematic source by applying also the proxy rake approximation has little effect compared to just using STF-Y2 with the complete moment tensor orientation information. Another interesting and important observation is that the similarity in waveforms and hence PGV values increases with growing distance from the epicenter (Fig. 16). We attribute this behavior to more complex on-fault source-time functions in the hypocentral region (Fig. 5) that are not well reproduced by either STF-Y1 or STF-Y2.

Further support to our observation that source-time function STF-Y2, coupled with a dip angle-based approximation of the rake angle distribution ("proxy rake"), reproduces not only the overall ground-motion patterns but also the seismic waveforms is given by the examples of rupture models D1i
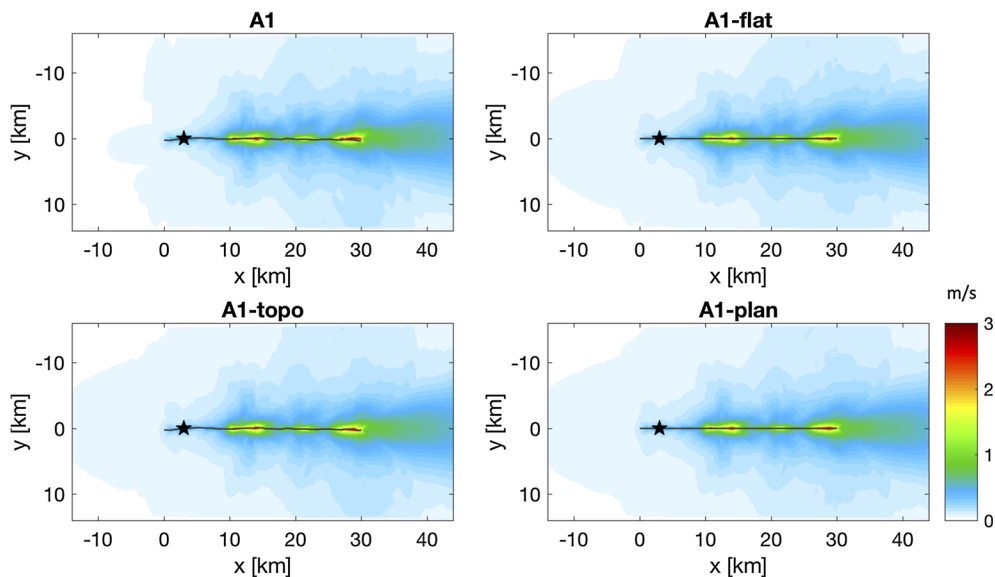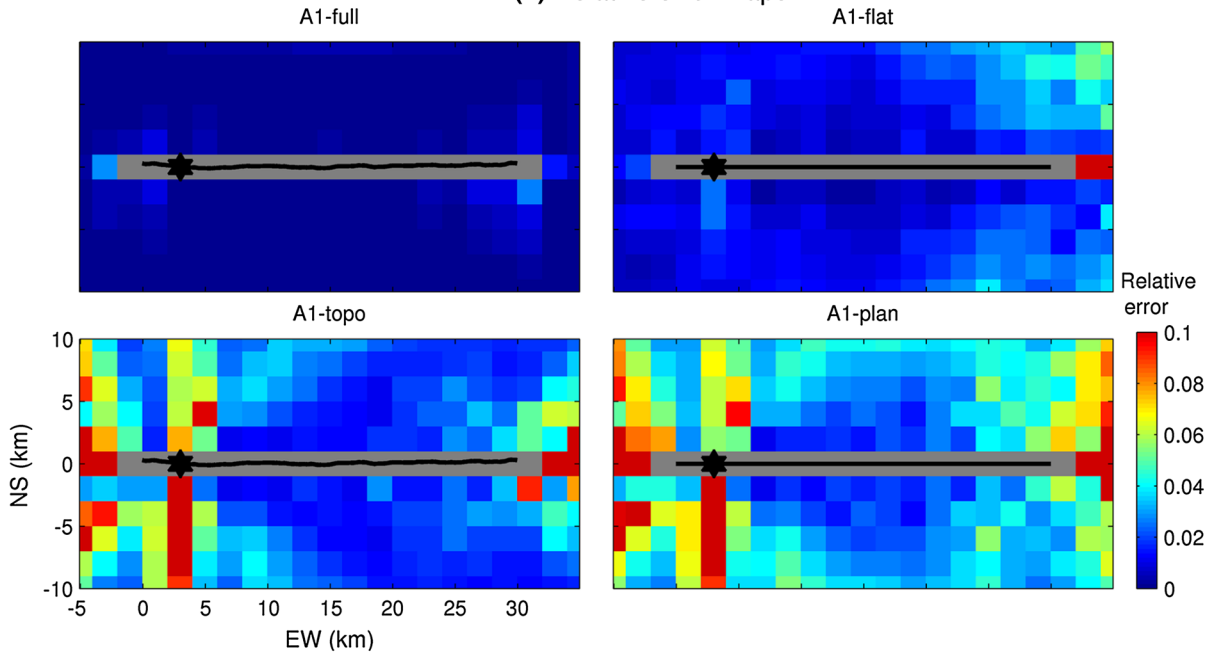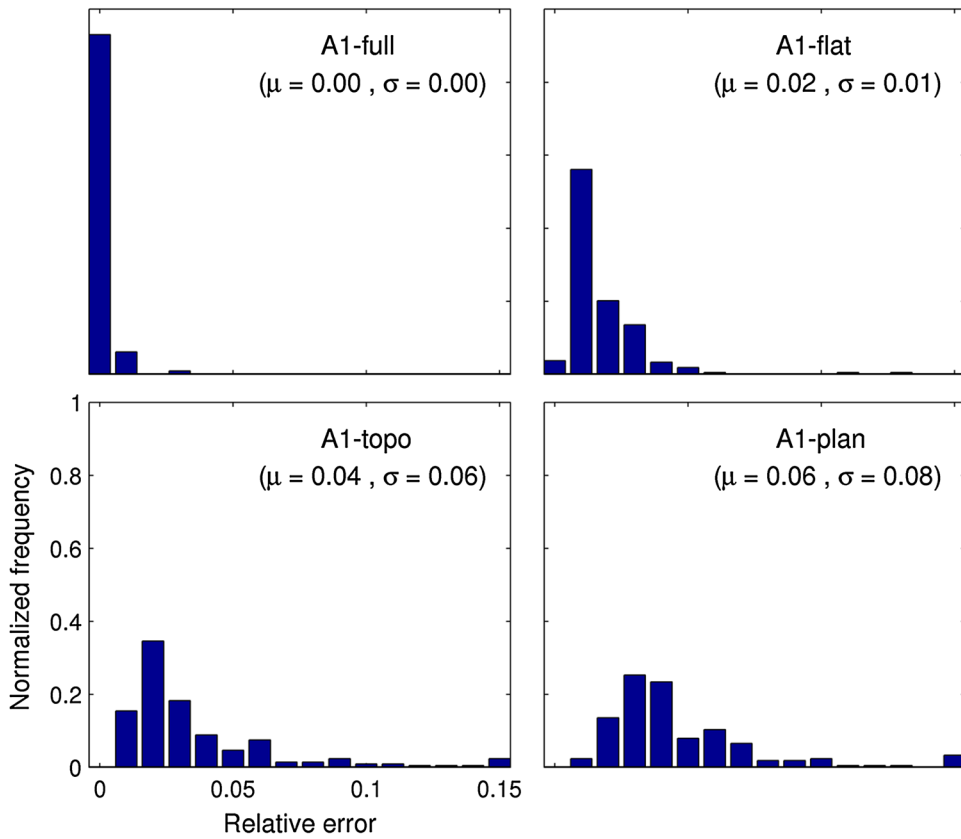

Figure 11

ShakeMaps of PGV, computed as GMRotD50 of the two horizontal components, for dynamic rupture scenario A1, and three kinematic models "topo," "flat," and "plan." The *black star* marks the hypocenter, the *black line* denotes the surface projection of the top edge of the fault, the color scale for PGV is given in m/s. Notice the strong shaking close to the fault, as well as the directivity effect in the forward direction of rupture propagation. These ShakeMaps illustrate the strong ground-motion similarities for all cases; however, we note that while planar representation A1-flat preserves asymmetric PGV distribution, A1-plan generates a symmetric shaking pattern

(a) Relative error maps

(b) Relative error histograms

◄Figure 12

a Maps of relative error (RE) for four kinematic models with respect to the dynamic model, indicating that A1-full and A1-flat well approximate the shaking levels of the dynamic rupture model A1. The *black line* denotes the surface projection of the top edge of the fault, the *star* shows the epicenter position. Very near-fault sites within the *gray shaded area* are not considered for computing the relative error. **b** Normalized frequency distributions of relative errors, normalized by total number of stations ($N = 214$)

and F1 (Table 1), shown in Figures S8 and S9 (Electronic Supplement). We also find that the near-fault Fourier amplitude spectra (in displacement) for the dynamic source models and their kinematic approximations follow an ω^{-2}-decay up to the highest resolved frequency ($f \sim 5.75$ Hz), with only minor spectral differences near this limiting frequency (Figures S10–S12).

5. *Correlation of Kinematic Source Parameters*

Pseudo-dynamic (PD) source modeling is based on the assumption that physical and/or empirical relations can be developed that link kinematic source properties to known or synthesized rupture quantities. For example, slip heterogeneity can be modeled as spatial random field, showing fractal behavior (in case the k^{-2} model is invoked, e.g., Frankel 1991; Herrero and Bernard 1994; Gallovič and Brokešová 2004; Ruiz et al. 2015) following a von Karman distribution (e.g., Mai and Beroza 2002) or similar distributions (Lavallee et al. 2006; Gusev 2011). Linking the rise time and/or rupture speed (or variations thereof) to slip is a common approach in pseudo-dynamic approximations (e.g., Guatteri et al. 2004; Schmedes et al. 2010, 2013; Song et al. 2013; Graves and Pitarka 2016).

PD modeling typically starts by simulating a heterogeneous slip distribution over the assumed rupture area (whose dimensions may be constrained from source scaling relations for a specific target magnitude or specified through geological/geophysical data). Slip heterogeneity can then be modeled as a constrained random field, assuming for instance a von Karman distribution (using its power spectral density in the Fourier domain) with magnitude-dependent correlation length and the power spectral decay at

high wave numbers k. An alternative slip heterogeneity characterization uses a fractal model with a k^{-2} decay. Without further constraints, the resulting one-point statistics of on-fault slip values then obey Gaussian statistics, centered at the average fault slip. However, it has been argued that normally distributed slip might not be appropriate for real earthquakes (Lavallee et al. 2006; Gusev 2011; Song and Dalguer 2013), while a recent study shows that slip statistics from source inversion results are best described by a truncated exponential distribution (Thingbaijam and Mai 2016).

Once the total slip on the fault is synthesized, the remaining kinematic source parameters need to be quantified, that is, rupture velocity and rise time, where the particular definition of rise time depends on the selected source-time function. Additional quantities may be needed, for instance the peak slip velocity on the fault (PSV) or the time between rupture onset and when the peak slip rate is reached (called "acceleration time" by Tinti et al. 2005). Since static stress change in the fault is linked to dynamic source properties, but can also be easily computed from fault slip (Ripperger and Mai 2004), it is often used in PD modeling (e.g., Guatteri et al. 2004). Final slip, static stress drop as well as correlations among rupture quantities are then used to generate a complete set of kinematic source parameters needed for ground-motion simulations (Guatteri et al. 2004; Schmedes et al. 2010; Mena et al. 2012; Song et al. 2013).

To examine how our rough fault dynamic rupture simulations may help improving pseudo-dynamic rupture characterizations, we briefly investigate the spatial interdependence of the kinematic source parameters extracted from the dynamic rupture models. In our analysis, we exclude the nucleation zone, and also points on the fault associated with locally occurring super-shear rupture speed. Furthermore, we extract the kinematic source quantities from the dynamic source-time function (STF-D) and from the slip-preserving Yoffe-type approximation STF-Y2. Figure 17 shows point densities for dynamic model A1, applying both STF-D and STF-Y2, when plotting slip against rise time, slip against rupture velocity, and peak slip velocity (PSV) against rupture velocity. We observe a nonlinear monotonic

(a) Model bias maps
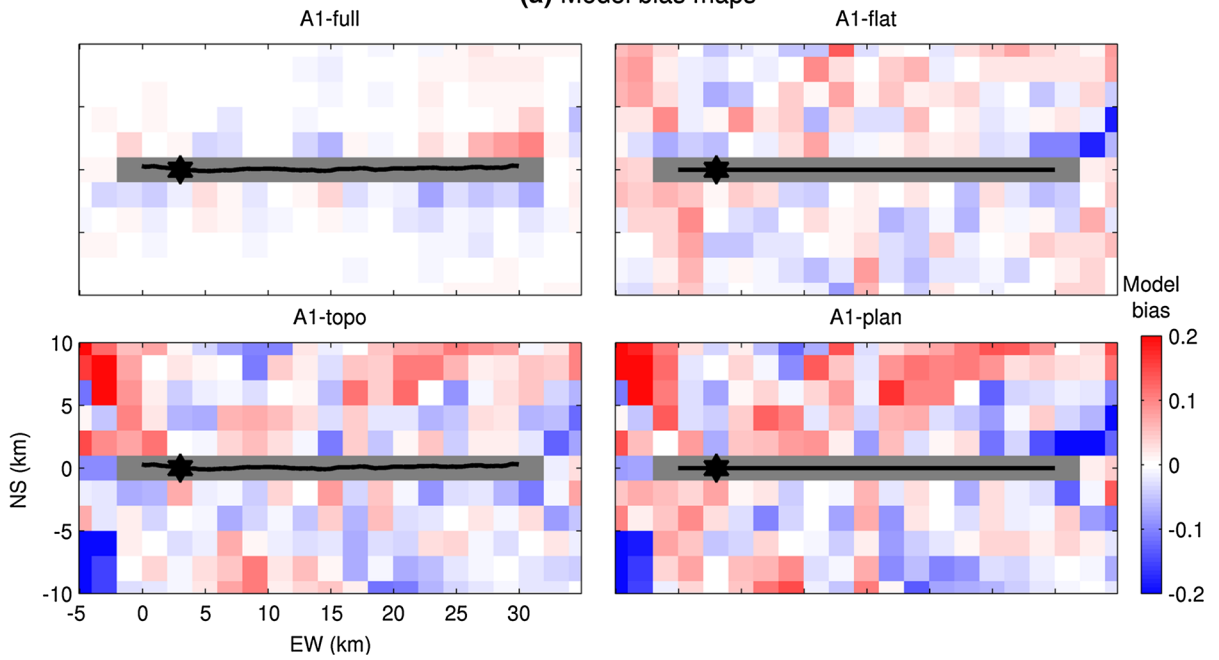
(b) Model bias histograms
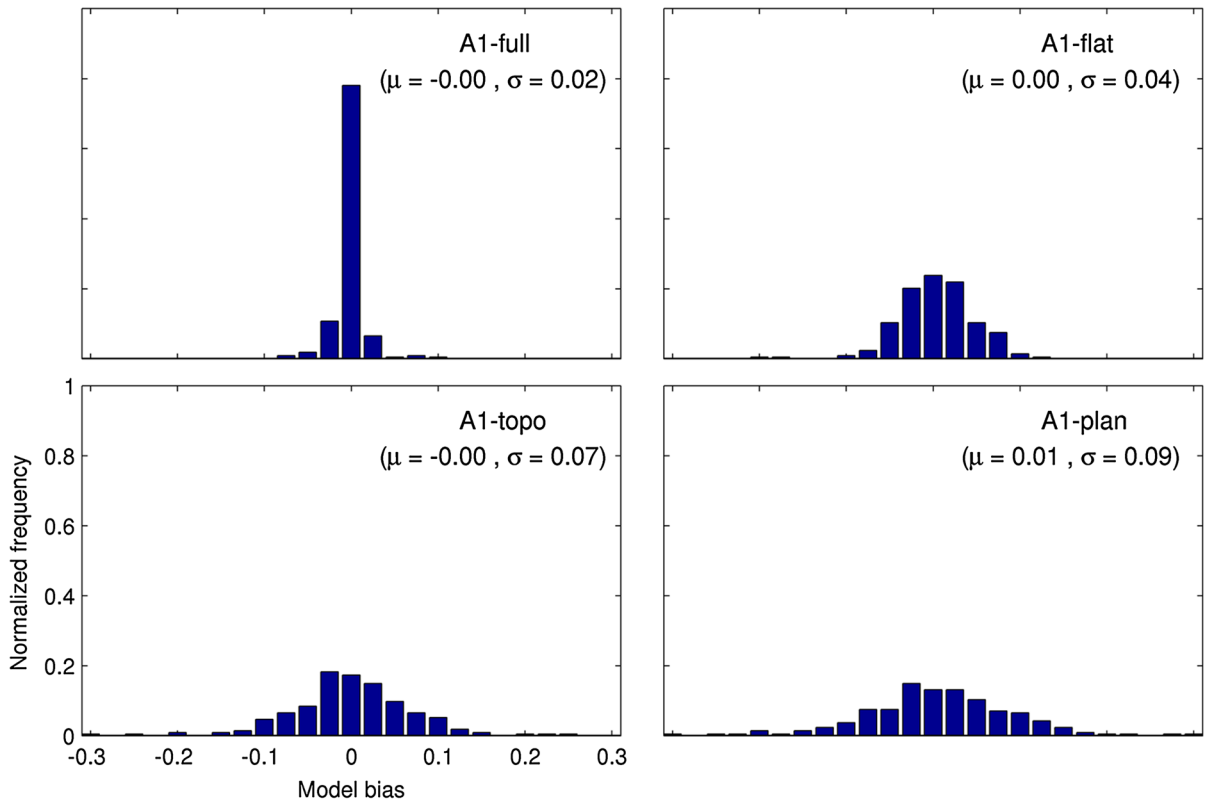
◀Figure 13
a Maps of model bias for four kinematic models with respect to the dynamic model, documenting that A1-full and A1-flat reproduce the shaking levels of the dynamic rupture model A1. The *black line* denotes the surface projection of the top edge of the fault; the *star* shows the epicenter position. Very near-fault sites within the *gray shaded area* are not considered for computing the model bias. **b** Normalized frequency distributions of relative errors, normalized by total number of stations ($N = 214$)

relationship between final slip and rise time. Longer rise times for a given slip value are found only for a small number of points on the fault, corresponding to STF-D's with trailing low-velocity slip (Fig. 5). No correlation exists between final slip and rupture velocity, but we find a positive correlation between

peak slip velocity and rupture velocity. Applying the STF-Y2 approximation compresses the point densities and sharpens the nonlinear scaling between slip and rise time and between peak slip velocity and rupture velocity.

To further explore such correlations between kinematic parameters, Fig. 18 displays log–log scatter plots between slip, peak slip velocity, rise time, rupture velocity, and acceleration time, extracted from the on-fault STF-D's for model A1. Here, we indicate also the correlation coefficient and the slope of a line, applying an orthogonal regression on the data only if the correlation coefficient is above 0.4 or below −0.4. The corresponding plot using STF-Y2 is
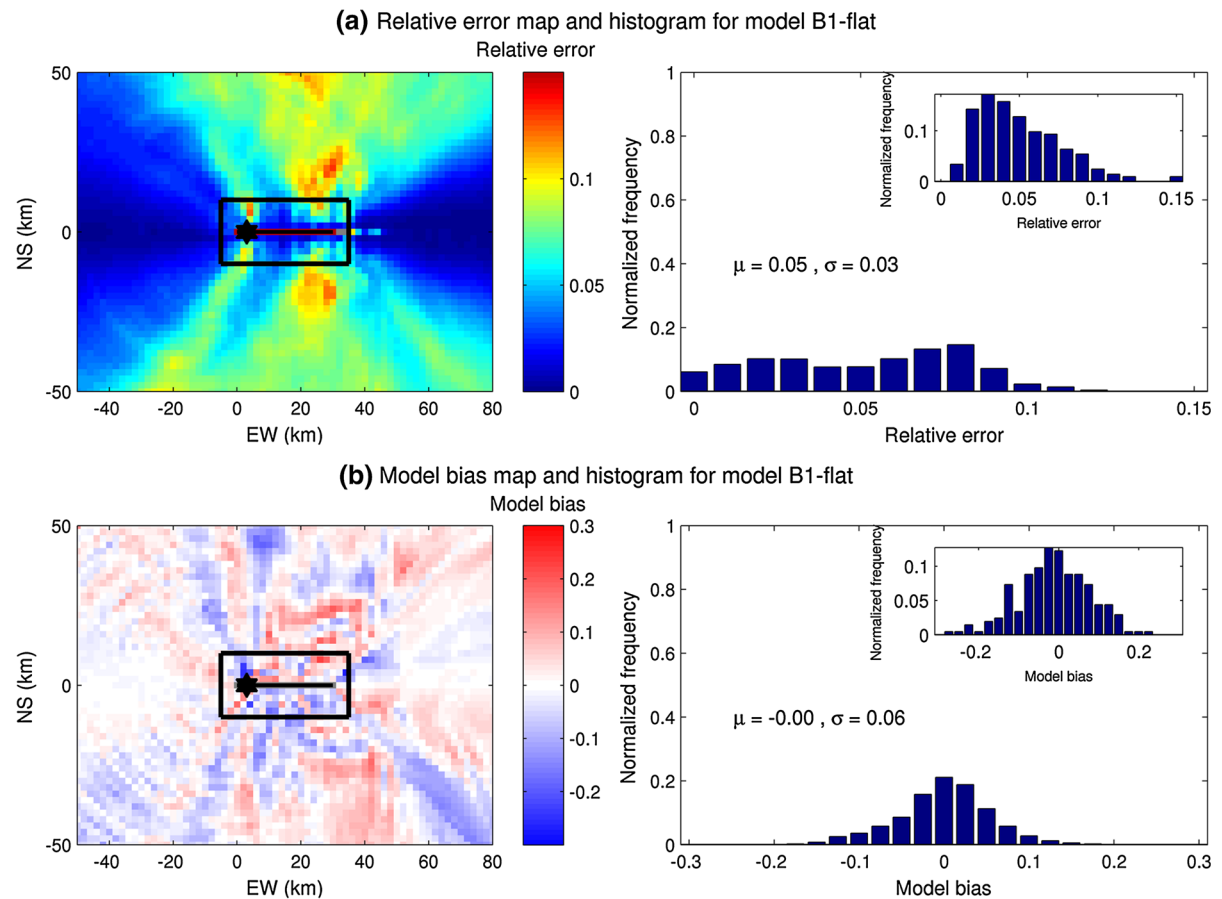

Figure 14
Ground-motion comparison for model B1 and B1-flat, showing **a** the map of relative error and its normalized frequency distribution, and **b** the map of model bias and its normalized frequency distribution. The relative error and model bias frequencies are normalized by total number of stations ($N = 3350$). The *black line* marks the fault trace; the *star* shows the epicenter position. Sites within the *gray shaded area* around the fault are not considered for computing the absolute error and model bias (see text for details). The histograms *insets* show the normalized frequency distribution for RE and MB values in the small region around the fault (*black rectangle*) that is identical to the area analyzed for model A1 in Figs. 12 and 13
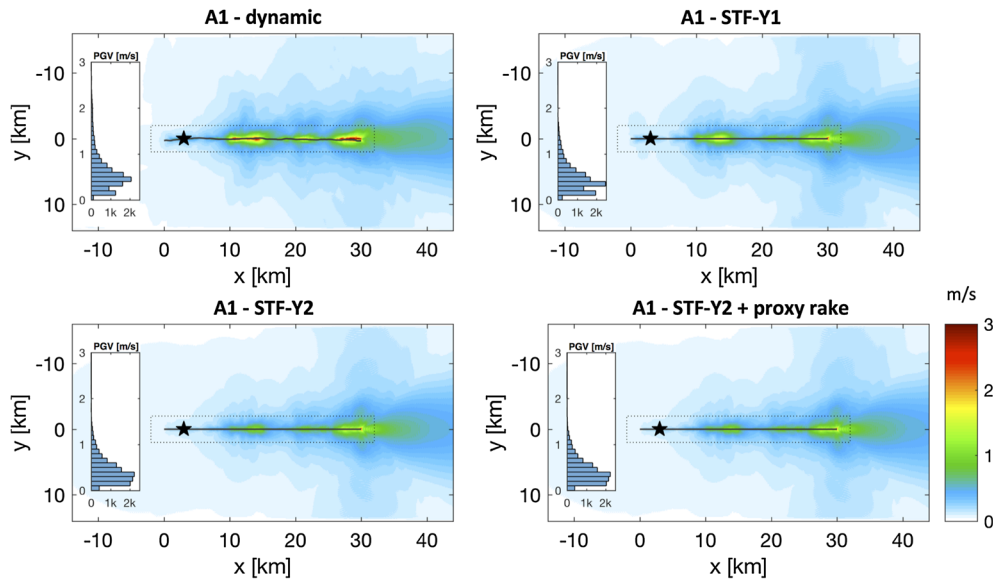
Figure 15
ShakeMap comparison of GMRotD50 of PGV for the dynamic source and kinematic sources with slip rate constrained (STF-Y1) and slip-preserving source-time functions (STF-Y2). For STF-Y2, we also present results with the approximated on-fault rake distribution (Fig. 7). The *insets* show PGV histograms for the region inside the *dotted rectangle* that covers a 2-km-wide swath around the fault trace. Even very close to the fault, PGV values are largely smaller than 1 m/s. Note the overall similarity in ground-motion patterns and PGV statistics

shown in the Electronic Supplement (Figure S13). We observe strong correlation with slip and rise time, but all other parameters are uncorrelated to slip. Rise time is anti-correlated to peak slip velocity, but weakly correlates with acceleration time. The strongest correlations (or anti-correlations) are found between rupture velocity, acceleration time and peak slip rate, in that high rupture speed leads to a short acceleration time and high peak slip velocity. These observations are qualitatively consistent with previous studies on dynamic ruptures on planar faults using different friction laws and/or inhomogeneous initial stress (Day 1982; Bizzarri 2012; Song and Dalguer 2013), and including plasticity (Gabriel et al. 2013).

To understand these observed correlations, we explore the shape of source-time functions in the context of the dynamic rupture process. Due to the rapid breakdown process at the crack tip, dynamic source-time functions generally show a sharp increase in slip velocity until the peak slip rate is reached. After peak slip is reached, a rapid decline occurs that transitions into a slow decay as the crack is sliding at the dynamic friction level. During the initial acceleration time, slip velocity increases almost linearly; therefore, a linear correlation can be expected between peak slip velocity and the acceleration time. The power law decay of slip velocity will result in a nonlinear relationship between final slip and rise time. Given the nonlinearity of the dynamic STFs, it is unlikely that slip correlates with either peak slip velocity or acceleration time. Note also that the physical processes during rupture that govern the decreasing slip velocity from its peak are significantly different from those controlling the initial rise of slip. Rupture velocity does not directly affect rupture arrest and hence does not correlate with rise time or final slip. Furthermore, by definition acceleration time is limited by rise time, which becomes important especially for shorter rise time. This effect could introduce an apparent positive correlation between the two parameters. Consequently, peak slip velocity may appear negatively correlated with rise time.

It is beyond the scope of this study to conduct further statistical analyses of all possible correlations between the kinematic source parameters extracted from the dynamic rupture simulations we have presented here (Table 1). This analysis is currently being undertaken and will be the focus of a forthcoming
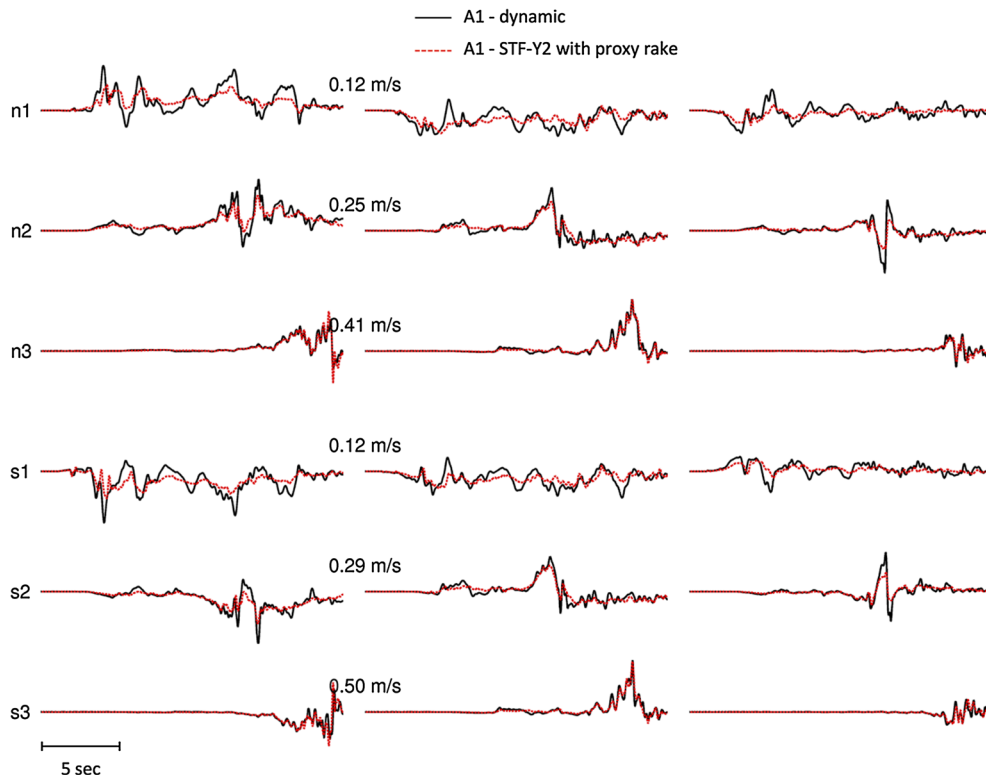
Figure 16

Velocity seismograms (in m/s) for the dynamic rupture model A1 (*black*) and the approximate kinematic source based on the STF-Y2 source-time functions and the proxy rake on a flat fault. Notice the waveform similarity and comparable peak ground velocities of the highly simplified kinematic source (see also Fig. 15). We find that waveform similarity increases with growing distance from the epicenter, due to more complex source-time functions in the hypocentral region

publication. However, it is interesting to point out that the strong (anti-) correlations among the temporal source parameters (rise time, rupture speed, acceleration time) and peak slip rate help to define the characteristics of the source-time function from which then the total slip can be constrained. We hypothesize that relating the spatial on-fault distribution of the kinematic source properties back to the underlying roughness patterns (e.g., Trugman and Dunham 2014) will help to develop a more comprehensive and physically self-consistent pseudo-dynamic rupture characterization.

6. Discussion

The results shown are based on numerically simulating the dynamic rupture process and its associated near-field seismic radiation for several realizations of fractally rough fault surfaces. We deliberately neglect other physical processes and features of real earthquakes to isolate the effects of fault roughness. For instance, larger-scale fault segmentation has been shown to strongly affect rupture dynamics and resulting shaking (e.g., Aochi and Madariaga 2003; Aochi and Douglas 2006; Oglesby et al. 2008; Oglesby and Mai 2012; Aochi and Ulrich 2015). Combining fault roughness with fault segmentation would be a natural extension of the work presented here. We have also ignored variations in Earth structure and Earth's surface topography to not obfuscate source effects with intricate wave propagation effects due to seismic scattering (e.g., Hartzell et al. 2010; Imperatori and Mai 2013, 2015; Graves and Pitarka 2016). Spatially variable initial stress (e.g., Ripperger et al. 2007) is not considered either, like any other variability in the initial conditions for rupture (e.g., friction, slip-weakening distance, rock
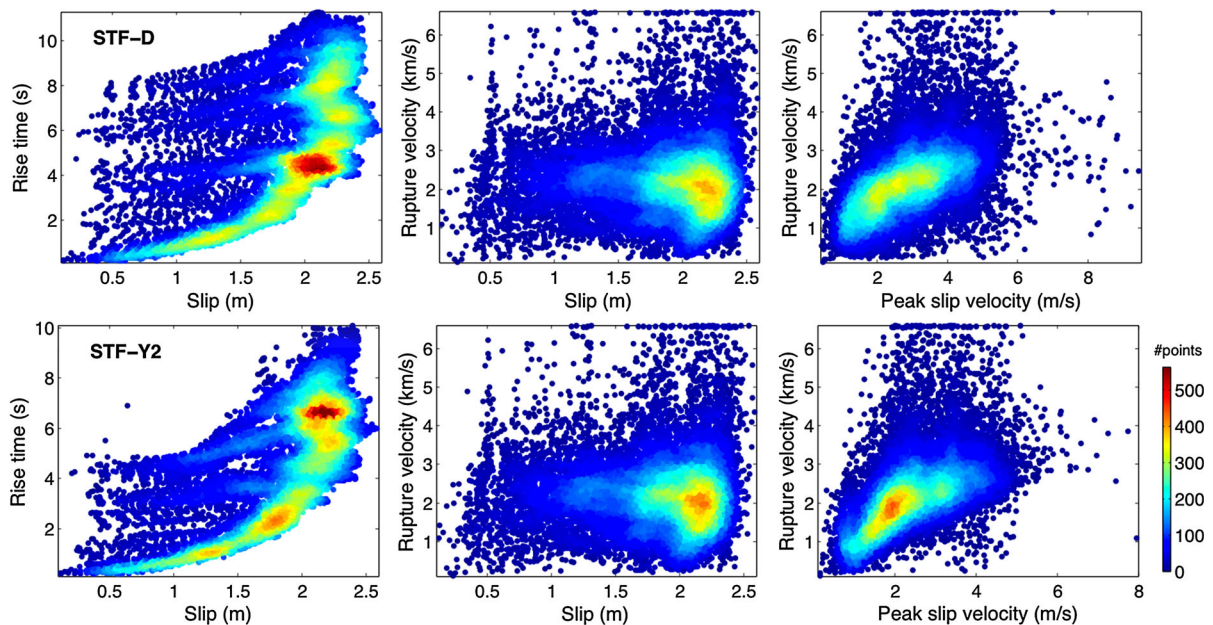
Figure 17

(*Top panels*) Correlations of kinematic source parameters obtained directly from dynamic rupture model A1 using its STF-D, showing total slip versus rise time (*left*), total slip versus local rupture velocity (*center*), and peak slip velocity versus rupture velocity (*right*). Data point density is given by the *color bar*. (*Bottom panel*) Same as above, but using the kinematic source-time function approximation STF-Y2

strength, or 3D fault zone structure). We have also restricted ourselves to strike-slip scenarios of magnitude $M \sim 7$ on a rupture plane of 30 km $\times$ 15 km, thus limiting the ability of the rupture to transition to super-shear rupture speeds. Thus, our results cannot be immediately extended/applied to very large (or long) strike-slip scenarios that are more prone to exhibit super-shear rupture velocity (e.g., Gabriel et al. 2012).

We remark that presently our rough-fault dynamic simulations do not reproduce the slip heterogeneity seen in finite-fault inversion. Instead of generating isolated strong slip patches, the dynamic simulations lead to slip maps resembling the underlying roughness pattern. When assuming spatially variable stress (e.g., Oglesby and Day 2002; Ripperger et al. 2007; Schmedes et al. 2010), the dynamic rupture simulations lead to complex rupture propagation, but rather smooth final on-fault slip. We conjecture that multi-scale roughness and/or stress heterogeneity is needed to reproduce slip variability as seen in fault slip inversions.

The ground-motion levels generated by our simulations generally capture the expected behavior in

terms of median and standard deviation when compared to a ground-motion prediction equation (e.g., Boore and Atkinson 2008; Figure S14), despite the simplifications and approximations in the modeling parameterization. However, we note that PGV values (in terms of GMRotD50) are particularly high in the very-fault region, while ground-motion variability appears to be distance-dependent, as reported in recent studies (Rodriguez-Marek et al. 2013; Vyas et al. 2016). We find largest PGV amplitudes very close to the surface trace of the fault (typically less then ~ 1 km away), reaching locally values of ~ 3 m/s (e.g., Figs. 11, 15, S8, S9). These are higher values than reported by Anderson (2012) for a global near-source strong-motion dataset that suggests peak ground velocities are mostly below ~ 2 m/s. Because strong-motion databases are still limited in the very near-fault region, the sampling bias for real earthquakes may contribute to this discrepancy. However, very large near-field motions in our simulations are partially also an effect of omitting seismic scattering that leads to a reduction and redistribution of peak motions (e.g., Imperatori and Mai 2013, 2015).
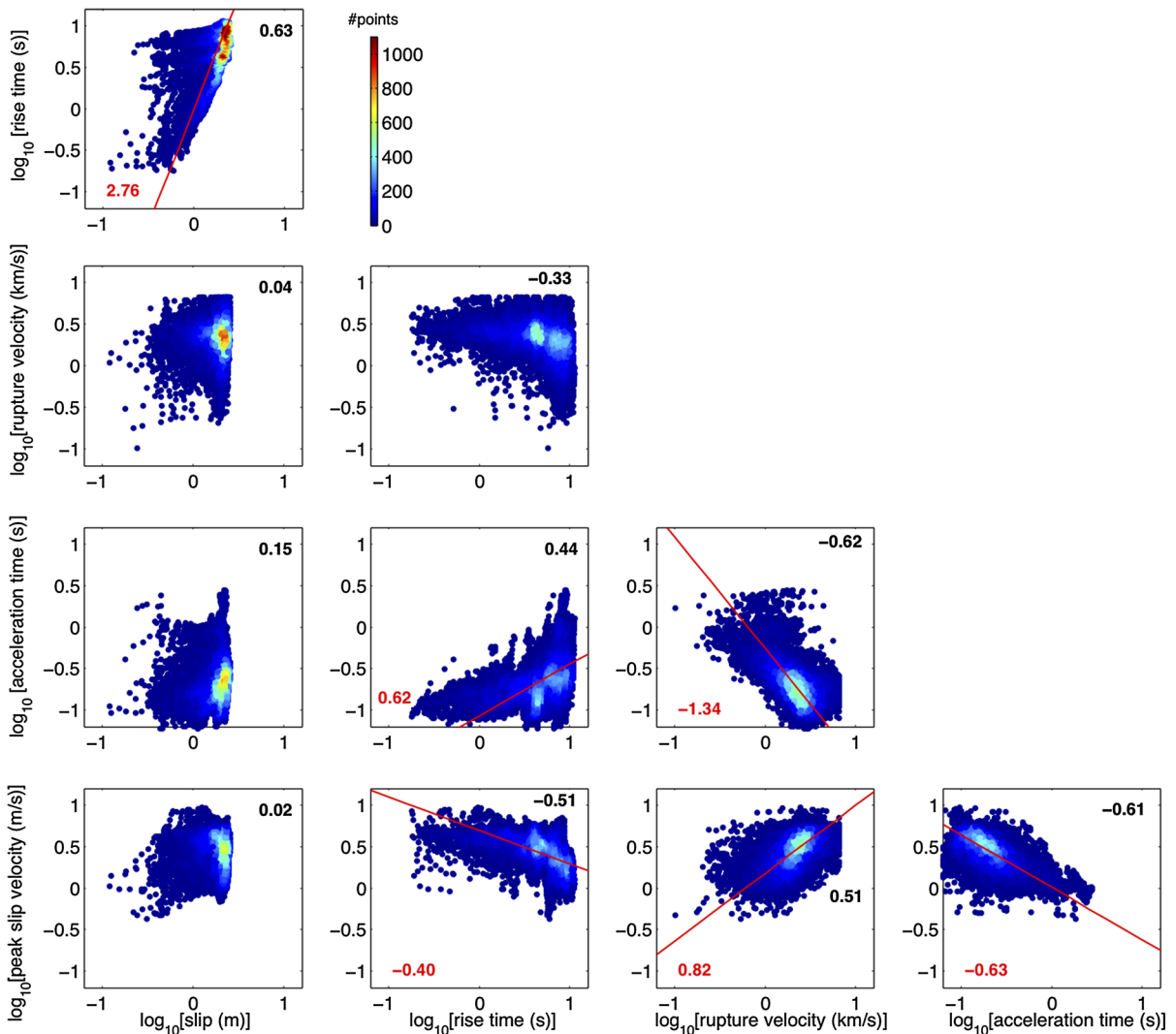
Figure 18
Correlation analysis between kinematic rupture parameters, extracted from the dynamic source-time functions (STF-Ds). Final slip correlates positively with rise time, but does not correlate with rupture velocity, acceleration time, and peak slip velocity. Rise time does not correlate with rupture velocity, but exhibits positive correlation with acceleration time and negative correlation with peak slip velocity. Rupture velocity correlates positively with peak slip velocity and negatively with acceleration time. Acceleration time shows negative correlation with peak slip velocity. *Black numbers* (*top right corner* in each *panel*) indicate the correlation coefficient; the *red values* (*bottom left corner*) states the slope of the regression line (*in red*) obtained from an orthogonal least-squares regression fit

In this study, plastic deformation in the medium is not included; likewise, we do not account for visco-elastic attenuation. We also use a simple linear slip-weakening friction law, instead of a more realistic rate-and-state law. Dunham et al. (2011) and Shi and Day (2013) discuss the importance of off-fault plasticity and strongly rate-weakening friction for simulating rough-fault dynamic ruptures. Roten et al.

(2014) document the effects of fault zone plasticity and attenuation on ground motions. However, we conjecture that the overall rupture evolution and the ground motions will not change dramatically if off-fault plasticity is included. To justify this, we estimated the spatial extent and duration of plastic yielding by evaluating the Mohr–Coulomb failure criterion at points near the fault on the free surface.

We set cohesion to zero and chose an internal friction coefficient of 0.7, which is only slightly higher than the static friction coefficient on the fault. The results of this computation (Electronic Supplement, Figure S15) imply that yielding would be confined to fault-perpendicular distances less than $\sim$1 km, with the yield criterion being violated only for about 0.5 s (exceeding 1 s only at few points) near the propagating rupture front. This observation leads us to conclude that our overall findings are not affected by omitting plasticity.

To examine further how plasticity may affect the ground motions, we conduct a set of simulations in which the on-fault slip rates are clipped at 6 m/s, using an approach similar to Andrews (2005). We apply the "flat-fault" approximation and the proxy rake, but insert the dynamic source-time functions (STF-D), limited to a peak slip rate of 6 m/s, into the kinematic simulations. We find that PGV reductions are confined to a small area near the fault. The ShakeMaps are virtually indistinguishable, while seismic waveforms at stations s1–s3 and n1–n3, located 4 km away from the fault, remain essentially unaffected by the artificially reduced slip rates (Electronic Supplement, Figures S16–S18, showing simulations for models A1, D1i, and F1 with clipped slip rate). This test also provides further support that the smoothed source-time function STF-Y2, for which on-fault peak slip rates are reduced by $\sim$10–25% (for models A1, D1i, F1), together with a flat-fault representation that honors the moment tensor orientation, are well suited to develop a new pseudo-dynamic rupture modeling method.

7. Conclusions

The surfaces of natural faults are characterized by out-of-plane topographic variations (so-called roughness) across a broad spectrum of lengths scales. Fault roughness strongly influences the dynamic rupture process, and with that also the resulting near-source seismic wavefield. Through dynamic rupture simulations, we investigate how different roughness parameterizations affect rupture evolution. Keeping all modeling parameters identical but inducing a small increase in roughness profoundly alters the rupture propagation and distribution of peak slip rates

(e.g., compare models A1 and B1, Table 1; Figs. 3, 4), and consequently also the near-field ground motions. We find that the roughness-induced rupture incoherence naturally generates high-frequency radiation that follows an ω^{-2}-decay. Therefore, broadband ground-motion simulations for earthquake engineering applications could profit greatly by including fault roughness, as it directly creates the desired ground-motion characteristics over the frequency range of interest in a fully physics-based approach.

However, dynamic rupture simulations are computationally expensive. We therefore test several planar fault kinematic source representations designed to emulate the observed dynamic behavior. Our results demonstrate that rough-fault source dynamics can be approximated in kinematic ground-motion simulations by retaining the moment tensor orientations but neglecting their off-fault positions. This is an important conclusion, because planar fault kinematic simulations are not only computationally simpler and cheaper, but there are also many well-tested and calibrated forward modeling codes for this purpose.

Testing various approximations to the local on-fault source-time functions of the dynamic simulations (STF-D), we define two Yoffe-type slip rate functions, STF-Y1 (slip rate constrained) and STF-Y2 (slip-preserving). Both STF-Y approximations reproduce the near-source seismic wavefield generated by the dynamic simulations, although the performance of STF-Y2 is statistically slightly preferable.

Finally, we observe that dynamic rake angle variations are anti-correlated to local dip angles, leading us to develop the "proxy rake" characterization using a low-pass-filtered and scaled dip angle distribution. Importantly, the ground motions resulting from corresponding "flat-fault proxy rake" kinematic simulations still very well reproduce the dynamically generated seismic wavefield.

In summary, our findings pave the way for a new pseudo-dynamic rupture modeling approach that captures effects of rough-fault source dynamics. Honoring the moment tensor orientations but neglecting their off-fault positions, and combining the known strike and dip angles with the dip angle

constrained "proxy rake" provides a very effective flat-fault characterization for kinematic ground-motion simulations. In addition, the slip-preserving Yoffe-type source-time function (STF-Y2) captures the essential features of the dynamic source-time function, whereby peak values of slip rate are reduced which appears to mimic plasticity effects on ground motions (reduction of near-fault shaking). Finally, we remark that our proposed kinematic rupture approximations do not change the frequency content of the radiated seismic wavefield (compared to the dynamic simulations), and therefore faciliates cost-effective broadband ground-motion computations for realistic simulation-based seismic hazard assessment.

Acknowledgements

References

Akkar, S., Sandıkkaya, M. A., Şenyurt, M., Azari, Sisi A., Ay, B. Ö., Traversa, P., et al. (2014). Reference database for seismic ground-motion in Europe (RESORCE). *Bulletin of Earthquake Engineering, 12,* 311–339.

Ancheta, T. D., Darragh, R. B., Stewart, J. P., Seyhan, E., Silva, W. J., BrianChiou, S.-J., et al. (2014). NGA-West2 database. *Earthquake Spectra, 30,* 989–1005.

Anderson, J.G. (2012). An overview of the largest amplitudes in recorded ground motions. In *Proceedings of the 15th World Conference of Earthquake Engineering (15 WCEE), Lisbon (Portugal),* Sept 24–28.

Anderson, J. G., & Brune, J. N. (1999). Probabilistic seismic hazard assessment without the ergodic assumption. *Seismological Research Letters, 70,* 19–28.

Andrews, D. J. (1976a). Rupture propagation with finite stress in antiplane strain. *Journal Geophysical Research, 81,* 3575–3582.

Andrews, D. J. (1976b). Rupture velocity of plane strain shear cracks. *Journal Geophysical Research, 81*(5679), 5687.

Andrews, D. J. (2005). Rupture dynamics with energy loss outside the slip zone. *Journal of Geophysical Research, 110,* B01307. doi:10.1029/2004JB003191.

Aochi, H., & Douglas, J. (2006). Testing the validity of simulated strong ground motion from the dynamic rupture of a fault system, by using empirical equations. *Bulletin of Earthquake Engineering, 4,* 211–229.

Aochi, H., & Madariaga, R. (2003). The 1999 Izmit, Turkey, earthquake: Nonplanar fault structure, dynamic rupture process and strong ground motion. *Bulletin of the Seismological Society of America, 93,* 1249–1266.

Aochi, H., & Ulrich, T. (2015). A Probable Earthquake 399 Scenario near Istanbul Determined from Dynamic Simulations. *Bulletin of the Seismological Society of America, 105,* 1468–1475. doi:10.1785/0120140283.

Atkinson, G. M., Assatourians, K., Boore, D. M., Campbell, K., & Motazedian, D. (2009). A guide to differences between stochastic point-source and stochastic finite-fault simulations. *Bulletin of the Seismological Society of America, 99,* 3192–3201.

Ben-Zion, Y., & Sammis, C. G. (2003). Characterization of fault zones. *Pure and Applied Geophysics, 160,* 677–715. doi:10.1007/PL00012554.

Bistacchi, A., Griffith, W. A., Smith, S. A. F., Di Toro, G., Jones, R., & Nielsen, S. (2011). Fault roughness at seismogenic depths from LIDAR and photogrammetric analysis. *Pure and Applied Geophysics.* doi:10.1007/s00024-011-0301-7.

Bizzarri, A. (2012). Rupture speed and slip velocity: What can we learn from simulated earthquakes? *Earth and Planetary Science Letters, 317,* 196–203.

Bommer, J. J., & Abrahamson, N. A. (2006). Why do modern probabilistic seismic-hazard analyses often lead to increased hazard estimates? *Bulletin of the Seismological Society of America, 96,* 1967–1977.

Bommer, J. J., Douglas, J., Scherbaum, F., Cotton, F., Bungum, H., & Fäh, D. (2010). On the selection of ground-motion prediction equations for seismic hazard analysis. *Seismological Research Letters, 81*(5), 783–793.

Boore, D. M., & Atkinson, G. M. (2008). Ground-motion prediction equations for the average horizontal component of PGA, PGV, and 5%-damped PSA at spectral periods between 0.01 s and 10.0 s. *Earthquake Spectra, 24*(1), 99–138.

Boore, D. M., Watson-Lamprey, J., & Abrahamson, N. A. (2006). Orientation independent measures of ground motion. *Bulletin of the Seismological Society of America, 96*(4A), 1502–1511. doi:10.1785/0120050209.

Bora, S. S., Scherbaum, F., Kuehn, N., & Stafford, P. (2014). Fourier spectral-and duration models for the generation of response spectra adjustable to different source-, propagation-, and site conditions. *Bulletin of Earthquake Engineering, 12*(1), 467–493.

Bozorgnia, Y., et al. (2014). NGA-West2 research project". *Earthquake Spectra, 30,* 973–987.

Brune, J. N. (1970). Tectonic stress and the spectra of seismic shear waves from earthquakes. *Journal Geophysical Research, 76,* 5002.

Campbell, W. K. (2003). Prediction of strong ground motion using the hybrid empirical method and its use in the development of ground-motion (attenuation) relations in Eastern North America. *Bulletin of the Seismological Society of America, 93*(3), 1012–1033.

Candela, T., Renard, F., Bouchon, M., Brouste, A., Marsan, D., Schmittbuhl, J., et al. (2009). Characterization of fault roughness at various scales: Implications of three-dimensional high resolution topography measurements. *Pure and Applied Geophysics, 166,* 1817–1851. doi:10.1007/s00024-009-0521-2.

Candela, T., Renard, F., Klinger, Y., Mair, K., Schmittbuhl, J., & Brodsky, E. E. (2012). Roughness of fault surfaces over nine decades of length scales. *Journal Geophysical Research, 117,* B08409. doi:10.1029/2011JB00904.

Causse, M., Cotton, F., & Mai, P. M. (2010). Constraining the roughness degree of slip heterogeneity. *Journal Geophysical Research, 115,* B05304. doi:10.1029/2009JB006747.

Causse, M., & Song, S. G. (2015). Are stress drop and rupture velocity of earthquakes independent? Insight from observed ground motion variability. *Geophysical Research Letters, 42*(18), 7383–7389.

Chiou, B., Darragh, R., Gregor, N., & Silva, W. (2008). NGA project strong-motion database. *Earthquake Spectra, 24,* 23–44.

Day, S. M. (1982). Three-dimensional simulation of spontaneous rupture: the effect of nonuniform prestress. *Bulletin of the Seismological Society of America, 72,* 1881–1902.

Delavaud, E., Scherbaum, F., Kuehn, N., & Allen, T. (2012). Testing the global applicability of ground-motion prediction equations for active shallow crustal regions. *Bulletin of the Seismological Society of America, 102,* 707–721.

Dreger, D., E. Tinti, & A. Cirella. (2007). Slip velocity function parameterization for broadband ground motion simulation, Seismological Society of America 2007 Annual Meeting Waikoloa, Hawaii, 11–13, April 2007.

Dunham, E. M., Belanger, D., Cong, L., & Kozdon, J. E. (2011). Earthquake ruptures with strongly rate-weakening friction and off-fault plasticity, Part 2: Nonplanar faults. *Bulletin of the Seismological Society of America, 10,* 2308–2322.

Ely, G. P., Day, S. M., & Minster, J.-B. (2008). A support-operator method for visco-elastic wave modeling in 3-D heterogeneous media. *Geophysical Journal International, 172,* 331–344.

Ely, G. P., Day, S. M., & Minster, J.-B. (2009). A support-operator method for 3-D rupture dynamics. *Geophysical Journal International, 177,* 1140–1150.

Frankel, A. (1991). High-frequency spectral fall-off of earthquakes, fractal dimension of complex rupture, b value, and the scaling of strength on faults. *Journal Geophysical Research, 96,* 6291–6302.

Gabriel, A. A., Ampuero, J.-P., Dalguer, L. A., & Mai, P. M. (2012). The transition of dynamic rupture modes in elastic media. *Journal Geophysical Research, 117*(B09311), 2012. doi:10.1029/2012JB009468.

Gabriel, A. A., Ampuero, J. P., Dalguer, L. A., & Mai, P. M. (2013). Source properties of dynamic rupture pulses with off-fault plasticity. *Journal Geophysical Research, 118,* 4117–4126. doi:10.1002/jgrb.50213.

Galis, M., Pelties, C., Kristek, J., Moczo, P., Ampuero, J.-P., & Mai, P. M. (2015). On initiation of dynamic rupture propagation with linear slip-weakening friction. *Geophysical Journal International, 200,* 888–907.

Gallovič, F., & Brokešová, J. (2004). On strong ground motion synthesis with k^{-2} slip distributions. *Journal of Seismology, 8*(2), 211–224.

Graves, R. W., Joran, T. H., Callaghan, S., Deelman, E., Field, E., Juve, G., et al. (2011). CyberShake: A Physics-Based Seismic Hazard Model for Southern California. *Pure and Applied Geophysics, 168,* 367–381.

Graves, R. W., & Pitarka, A. (2010). Broadband ground-motion simulation using a hybrid approach. *Bulletin of the Seismological Society of America, 100*(5A), 2095–2123.

Graves, R., & Pitarka, A. (2016). Kinematic ground-motion simulations on rough faults including effects of 3D stochastic velocity perturbations. *Bulletin of the Seismological Society of America.* doi:10.1785/0120160088.

Guatteri, M., Mai, P. M., & Beroza, G. C. (2004). A pseudo-dynamic approximation to dynamic rupture models for strong ground motion prediction. *Bulletin of the Seismological Society of America, 94*(6), 2051–2063.

Gusev, A. A. (2011). Statistics of the values of a normalized slip in the points of an earthquake fault". *Izvestiya, Physics of the Solid Earth, 47,* 176–185.

Hartzell, S., Harmsen, S., & Frankel, A. (2010). Effects of 3D random correlated velocity perturbations on predicted ground motions. *Bulletin of the Seismological Society of America, 100*(4), 1415–1426. doi:10.1785/0120090060.

Hartzell, S. H., & Heaton, T. H. (1983). Inversion of strong ground motion and teleseismic waveform data for the fault rupture history of the 1979 Imperial Valley, California, earthquake. *Bulletin of the Seismological Society of America, 73,* 1553–1583.

Herrero, A., & Bernard, P. (1994). A kinematic self-similar rupture process for earthquake. *Bulletin of the Seismological Society of America, 84,* 1216–1228.

Ide, S. (2007). Slip inversion, in Treatise on Geophysics. In H. Kanamori (Ed.), *Earthquake Seismology*, vol. 4, (pp. 193–224). Amsterdam, The Netherlands: Elsevier. ISBN: 978-0-444-51932-0.

Imperatori, W., & Mai, P. M. (2013). Broadband near-field ground-motion simulations in 3-dimensional scattering media. *Geophysical Journal International, 92,* 725–744.

Imperatori, W., & Mai, P. M. (2015). The role of topography and lateral velocity heterogeneities on near-source scattering. *Geophysical Journal International, 202,* 2163–2181. doi:10.1093/gji/ggv281.

Kaeser, M., & Gallovic, F. (2008). Effects of complicated 3-D rupture geometries on earthquake ground motion and their implications: a numerical study. *Geophysical Journal International, 172,* 276–292. doi:10.1111/j.1365-246X.2007.03627.x.

Kluegel, J. U. (2007). Comment on "Why do modern probabilistic seismic-hazard analyses often lead to increased hazard estimates?" by Julian J. Bommer and Norman A. Abrahamson. *Bulletin of the Seismological Society of America, 97,* 2198–2207.

Kostrov, B. V. (1964). Self-similar problems of propagation of shear cracks. *Journal of Applied Mathematics and Mechanics, 28,* 1077–1087.

Lavallee, D., Liu, P., & Archuleta, R. J. (2006). Stochastic model of heterogeneity in earthquake slip spatial distributions. *Geophysical Journal International, 165,* 622–640.

Leonard, M. (2010). Earthquake fault scaling: Self-consistent relating of rupture length, width, average displacement, and

moment release. *Bulletin of the Seismological Society of America, 100,* 1971–1988.

Liu, P., Archuleta, R. A., & Hartzell, S. H. (2006). Prediction of broadband ground-motion time histories: Hybrid low/high-frequency method with correlated random source parameters. *Bulletin of the Seismological Society of America, 96*(6), 2118–2130.

Mai, P. M. (2009). Ground Motion: Complexity and Scaling in the Near Field of Earthquake Ruptures. In W. H. K. Lee & R. Meyers (Eds.), *Encyclopedia of Complexity and Systems Science* (pp 4435–4474). Springer.

Mai, P. M., & Beroza, G. C. (2000). Source scaling properties from finite-fault-rupture models. *Bulletin of the Seismological Society of America, 90,* 604–615.

Mai, P. M., & Beroza, G. C. (2002). A spatial random-field model to characterize complexity in earthquake slip. *Journal Geophysical Research.* doi:10.1029/2001JB000588.

Mai, P.M., Imperatori, W., & Olsen, K. B. (2010). Hybrid broadband ground-motion simulations: combining long-period deterministic synthetics with high-frequency multiple S-to-S backscattering. *Bulletin of the Seismological Society of America, 100,* 2124–2142. doi:10.1785/0120080194

Mai, P. M., & Thingbaijam, K. K. S. (2014). SRCMOD: An online database of finite-fault rupture models. *Seismological Research Letters, 85*(6), 1348–1357.

Mena, B., Dalguer, L. A., & Mai, P. M. (2012). Pseudo-dynamic source characterization for strike-slip faulting, including stress heterogeneity and super-shear rupture. *Bulletin of the Seismological Society of America, 102*(4), 1654–1680. doi:10.1785/0120110111.

Mena, B., Mai, P. M., Olsen, K. B., Purvance, M. D., & Brune, J. (2010). Hybrid broadband ground-motion simulation using scattering Green's functions: application to large-magnitude events. *Bulletin of the Seismological Society of America, 100*(5A), 2143–2162. doi:10.1785/0120080318.

Oglesby, D. D., & Day, S. M. (2002). Stochastic fault stress: Implications for fault dynamics and ground motion. *Bulletin of the Seismological Society of America, 92,* 3006–3021.

Oglesby, D. D., & Mai, P. M. (2012). Fault Geometry, rupture dynamics, and ground motion from potential earthquakes on the North Anatolian Fault Zone under the Sea of Marmara. *Geophysical Journal International.* doi:10.1111/j.1365-246X.2011.05289.x.

Oglesby, D. D., Mai, P. M., Atakan, K., & Pucci, S. (2008). Dynamic models of earthquakes on the North Anatolian fault under the Sea of Marmara: The effect of hypocenter location. *Geophysical Research Letters, 35,* L18302. doi:10.1029/2008GL035037.

Pardo-Iguzquiza, E., & Chica-Olmo, M. (1993). The Fourier integral method: an efficient spectral method for simulation of random fields. *Mathematical Geology, 25,* 177–217.

Power, M., Chiou, B., Abrahamson, N., Bozorgnia, Y., Shantz, T., & Roblee, C. (2008). An overview of the NGA project. *Earthquake Spectra, 24,* 3–21.

Power, W. L., & Tullis, T. E. (1991). Euclidean and fractal models for the description of rock surface roughness. *Journal Geophysical Research, 96,* 415–424.

Renard, F., Voisin, C., Marsan, D., & Schmittbuhl, J. (2006). High resolution 3-D laser scanner measurements of a strike-slip fault quantify its morphological anisotropy at all scales. *Geophysical Research Letters, 33,* L04305. doi:10.1029/2005GL025038.

Ripperger, J., Ampuero, J. P., Mai, P. M., & Giardini, D. (2007). Earthquake source characteristics from dynamic rupture with constrained stochastic fault stress. *Journal Geophysical Research, 112,* B04311. doi:10.1029/2006JB004515.

Ripperger, J., & Mai, P. M. (2004). Fast computation of static stress changes on 2D faults from final slip distributions. *Geophysical Research Letters, 31*(18), L18610. doi:10.1029/2004GL020594.

Ripperger, J., Mai, P. M., & Ampuero, J. P. (2008). Variability of near-field ground-motion from dynamic earthquake rupture simulation. *Bulletin of the seismological society of America, 98*(3), 1207–1228.

Rodriguez-Marek, A., Cotton, F., Abrahamson, N. A., Akkar, S., Al-Atik, L., Edwards, B., et al. (2013). A model for single-station standard deviation using data from various tectonic regions. *Bulletin of the seismological society of America, 103*(6), 3149–3163.

Roten, D., Olsen, K. B., Day, S. M., Cui, Y., & Fäh, D. (2014). Expected seismic shaking in Los Angeles reduced by San Andreas fault zone plasticity. *Geophysical Research Letters, 41*(8), 2769–2777.

Ruiz, J. A., Fuentes, M., Riquelme, S., Campos, J., & Cisternas, A. (2015). Numerical simulation of tsunami runup in northern Chile based on non-uniform k^{-2} slip distributions. *Natural Hazards, 79*(2), 1177–1198.

Sagy, A., & Brodsky, E. E. (2009). Geometric and rheological asperities in an exposed fault zone. *Journal Geophysical Research, 114,* B02301. doi:10.1029/2008JB005701.

Sagy, A., Brodsky, E. E., & Axen, G. J. (2007). Evolution of fault-surface roughness with slip. *Geology, 35*(3), 283–286. doi:10.1130/G23235A.1.

Schmedes, J., Archuleta, R. J., & Lavallée, D. (2010). Correlation of earthquake source parameters inferred from dynamic rupture simulations. *Journal Geophysical Research, 115,* B03304. doi:10.1029/2009JB006689.

Schmedes, J., Archuleta, R. J., & Lavallée, D. (2013). A kinematic rupture model generator incorporating spatial interdependency of earthquake source parameters. *Geophysical Journal International, 192,* 1116–1131. doi:10.1093/gji/ggs02.

Shi, Z., & Day, S. M. (2013). Rupture dynamics and ground motion from 3-D rough-fault simulations. *Journal Geophysical Research, 118*(3), 1122–1141. doi:10.1002/jgrb.50094.

Song, S. G., & Dalguer, L. A. (2013). Importance of 1-point statistics in earthquake source modelling for ground motion simulation. *Geophysical Journal International, 192,* 1255–1270.

Song, S.-G., Dalguer, L. A., & Mai, P. M. (2013). Pseudo-dynamic source modeling with 1-point and 2-point statistics of earthquake source parameters. *Geophysical Journal International, 196*(3), 1770–1786. doi:10.1093/gji/ggt479.

Song, S. G., & Somerville, P. (2010). Physics-based earthquake source characterization and modeling with geostatistics. *Bulletin of the Seismological Society of America, 100*(2), 482–496.

Spudich, P., & Xu, L. (2003). Software package COMPSYN: Programs for earthquake ground motion calculation using complete 1-D Green's functions, in International Handbook of Earthquake & Engineering Seismology. In W. H. K. Lee, H. Kanamori, P. Jennings, & C. Kisslinger (Eds.), *International Geophysics Series* (Vol. 81). Amsterdam: Academic Press.

Stewart, J. P., Douglas, J., Javanbarg, M., Bozorgnia, Y., Abrahamson, N. A., Boore, D. M., et al. (2015). Selection of ground motion prediction equations for the Global Earthquake Model. *Earthquake Spectra, 31,* 19–45.

Strasser, F. O., Abrahamson, N. A., & Bommer, J. J. (2009). Sigma: Issues, insights, and challenges. *Seismological Research Letters, 80,* 40–56.

Thingbaijam, K. K. S., & Mai, P. M. (2016). Evidence for truncated exponential probability distribution of earthquake slip. *Bulletin of the Seismological Society of America*. doi:10.1785/012015029.

Tinti, E., Fukuyama, E., Piatanesi, A., & Cocco, M. (2005). A kinematic source-time function compatible with earthquake dynamics. *Bulletin of the Seismological Society of America, 95,* 1211–1223.

Trugman, D. T., & Dunham, E. M. (2014). A 2D pseudo-dynamic rupture model generator for earthquakes on geometrically complex faults. *Bulletin of the Seismological Society of America, 104*(1), 95–112. doi:10.1785/0120130138.

Vyas, J. M., Galis, M., & Mai, P. M. (2016). Distance and azimuthal dependence of ground-motion variability. *Bulletin of the Seismological Society of America*. doi:10.1785/0120150298.

Wang, Z., & Zhou, M. (2007). Comment on "Why do modern probabilistic seismic-hazard analyses often lead to increased hazard estimates?" by Julian J. Bommer and Norman A. Abrahamson. *Bulletin of the Seismological Society of America, 97,* 2212–2221.

Yoffe, E. (1951). The moving Griffith crack. *Philosophical Magazine, 42,* 739–750.